Shock Waves (2020) 30:325–347
https://doi.org/10.1007/s00193-019-00927-x

ORIGINAL ARTICLE

Simulation-driven design of experiments examining the large-scale, explosive dispersal of particles

K. T. Hughes[1] · S. Balachandar[1] · A. Diggs[2] · R. Haftka[1] · N. H. Kim[1] · D. Littrell[2]

Received: 20 March 2019 / Revised: 9 September 2019 / Accepted: 21 September 2019 / Published online: 15 October 2019

Abstract
A series of six, large-scale tests were performed at the Eglin Air Force Base blastpad facility to serve as a validation benchmark for the explosive dispersal of particles. The series contained two baseline tests, one tungsten liner test, and three steel liner tests. Careful emphasis was placed on design of the experiments to allow ease of simulation, uncertainty quantification of experimental inputs, and extraction of prediction metrics. Design decisions, such as using a casing that is negligible to the flow, serve to greatly reduce the computational effort to perform validation. Attention is also paid to quantifying uncertainty in experimental inputs such as explosive density, particle size distribution, particle density, volume fraction, and ambient conditions. For each test, data were collected from four high-speed cameras, 54 inground pressure transducers, and eight unconfined momentum traps. From these diagnostics, prediction metrics are extracted measuring the shock time of arrival, peak pressure, impulse per unit area, and the contact/particle front position. The high-speed video shows significant differences between the steel and tungsten liners. The tungsten particles were incandescent as they dispersed and concentrated in a bright, dense band followed by alternating bright and dark striations. There was little to no incandescence in the dispersed steel particles. The steel liner tests exhibited instabilities with fine fingers racing ahead of the front. The instabilities, however, were so numerous that they are not easily distinguishable from each other, preventing their characterization.

Keywords Uncertainty quantification · Multiphase flow · Explosive · Validation · Explosive dispersal

1 Introduction

The experiments presented in this paper were conducted on July 19–28, 2017, at Eglin Air Force Base (Eglin AFB) under the guidance of Air Force Research Laboratory (AFRL) personnel Don Littrell and Angela Diggs, and the data made available for use. The problem of interest is a high-speed dispersal of an annular, dry particle bed driven by a core of reacting explosive. Many interesting and complex phenomena are present, including detonation chemistry, turbulence, particle collisions, drag forces, real gas effects, shock–particle interactions, and particle–gas contact interactions. On the one hand, these experiments serve as a test bed for exploring the rich physics of compressible multiphase instabilities and turbulence. On the other hand, the experiments play an important role in establishing a benchmark for validation of multiphase models developed to predict the shock and particle front location. While some parametric variation is employed, the contribution of this paper focuses on quantification of uncertainties in the experimental inputs, details of the experimental data processing, and uncertainty of the primary prediction metrics. Due to its intention as a validation data set, multiple tests of the same nominal configuration were performed and considerable care was taken to avoid unnecessary experimental complications where possible.

The present test series builds on a history of high-quality multiphase experiments. A series of previous, small-scale validation experiments have extracted the particle positions, velocities, and forces of individual particles when subjected to a shock. For example, experiments by Takayama and coworkers [1–3] used an accelerometer installed inside a sphere to measure the force on a particle at sub-microsecond resolution. Various investigators have also conducted microscale experiments in shock tubes where an isolated or a small col-

Communicated by D. Frost.

✉ N. H. Kim
nkim@ufl.edu

[1] Department of Mechanical and Aerospace Engineering, University of Florida, Gainesville, FL 32611, USA

[2] Air Force Research Laboratory, Munitions Directorate, Eglin Air Force Base, FL 32542, USA

lection of particles were allowed to move freely in response to forces exerted on them by the shock and the post-shock flow [4–7]. Hughes et al. [8] tracked the position of a small number of particles subjected to a detonation wave with the use of X-ray imaging. Wagner et al. [9] and DeMauro et al. [10] have conducted various investigations studying particle curtains interacting with a planar shock wave within a shock tube. Particle fronts were extracted with high-speed schlieren photography, while time-varying particle curtain volume fraction was obtained from X-ray imagery. Kellenberger et al. [11] performed similar investigations with increased volume fraction and a stationary fixed bed of particles.

Less prevalent are data sets for large-scale explosive dispersals. Frost, Zhang, and collaborators have conducted a series of pioneering experiments under varying test configurations to understand the nature of explosive dispersal of particles and the resulting instabilities of the rapidly advancing particle front through high-speed video analysis [12–14]. Milne et al. [15] have demonstrated for liquid layers that the fingering instability is largely insensitive to material properties but depends mostly on the mass loading. Pontalier et al. [16] have studied the attenuation of the pressure wave for various particle materials and mass loadings. Interestingly, Pontalier et al. show that solid particles are more effective than liquid layers at blast mitigation, suggesting that particle deformation, compaction, and collision are a significant source of energy loss. For an excellent discussion on the instabilities and their possible sources of formation, the interested reader is directed to Frost [17].

These large-scale experiments were largely focused on understanding the mechanisms underlying the instability present in the advancing material front or the blast wave mitigation. The number of diagnostics was limited, often utilizing a single high-speed camera, one-to-two X-ray exposures, and three-to-four far-field pressure transducers. The present goal is to employ a large number of simultaneous diagnostics to provide a rich data set for both uncertainty quantification and to serve as a benchmark for modeling and validation of future simulations. Similar levels of diagnostics have been used by Bai et al. [18] to study the inertial effects of a falling charge containing aluminum powder, fuel droplets, and fuel vapor. This investigation will present the results from a large number of diagnostics for the explosive dispersal of a cylindrical, annular particle bed and provide careful uncertainty quantification of the experimental parameters.

The remainder of this paper is organized as follows: Sect. 2 will detail the experimental setup, diagnostics, and test articles. A significant portion of the section will be dedicated to explaining design choices with regard to the mass loading of the test article, explosive material, casing, and so on. Section 3 will overview the uncertainty quantification of the experimental inputs. The processing of the results from the pressure probes, impulse diagnostic, and high-speed cameras will be presented in Sect. 4. Section 5 concludes the paper with a summary of the work.

2 Experimental setup

2.1 Experimental facility and diagnostics

The experiments were conducted at the AFRL blastpad, as shown in Fig. 1. The blastpad is an outdoor testing facility located at Eglin AFB consisting of a 42 m by 24 m concrete pad and exhaust pit. The inner 1.85 m of the pad is replaced with a cylindrical steel insert to better weather the explosive testing. During testing, the charge was oriented horizontally with the center axis placed flush with the ground. The charge was supported with a wooden frame and a Styrofoam cradle. When the test charge was detonated, the lower half of the resulting detonation was directed downward, turned, and then exhausted to a pit away from the blastpad. See Barreto et al. [19] for further details concerning the AFRL blastpad.

The instrument suite consisted of 54 inground Kulite HKS-37-375 series pressure transducers, four high-speed cameras, eight unconfined momentum traps (UMTs), and six optical linear encoders (OLEs). Each pressure probe was sampled at 1 MHz. The pressure probes were arranged in rays emanating from the center of the test article, as shown in Fig. 1a. A Pearson probe wrapped the detonation line to measure the detonation delay, also sampled at 1 MHz, and is used to align the pressure histories with the detonator initiation. The Pearson probe contains a Ragowski coil and measures the current derivative within the trigger line. During the course of the analysis, the angular location, θ, will sometimes be referenced for convenience and refers to the angle counterclockwise from the positive x-axis. For example, the Camera 3 axis in Fig. 1a is at 90° to the x-axis. Two Phantom v1212 cameras were placed on the 0° and 180° lines, referred to as Cameras 1 and 4, respectively. The remaining two perspectives were provided by Phantom v711 cameras placed at the 45° and 90°, referred to as Cameras 2 and 3, respectively. The Phantom v711 cameras were sampled at 7500 frames per second (fps), and the Phantom v1212 cameras were sampled at 12,000 fps. All four cameras were sampled at the full resolution of 1280 × 800 pixels.

Additionally, the eight UMTs were placed 1.45 m from the charge and elevated 46 cm on stands welded to the blastpad center insert. The UMTs measure the total, collective impulse of the gas and particles by measuring the throw distance of cylinders spaced at regular intervals around the explosive. The UMTs were solid aluminum cylinders 10.16 cm in diameter and 10.16 cm in length. The UMTs were spray painted with alternating colors and balanced on the stands. The UMTs have been previously used in tests of cylindrical charges as demonstrated by Held [20,21]. Contrary to the work of Held,

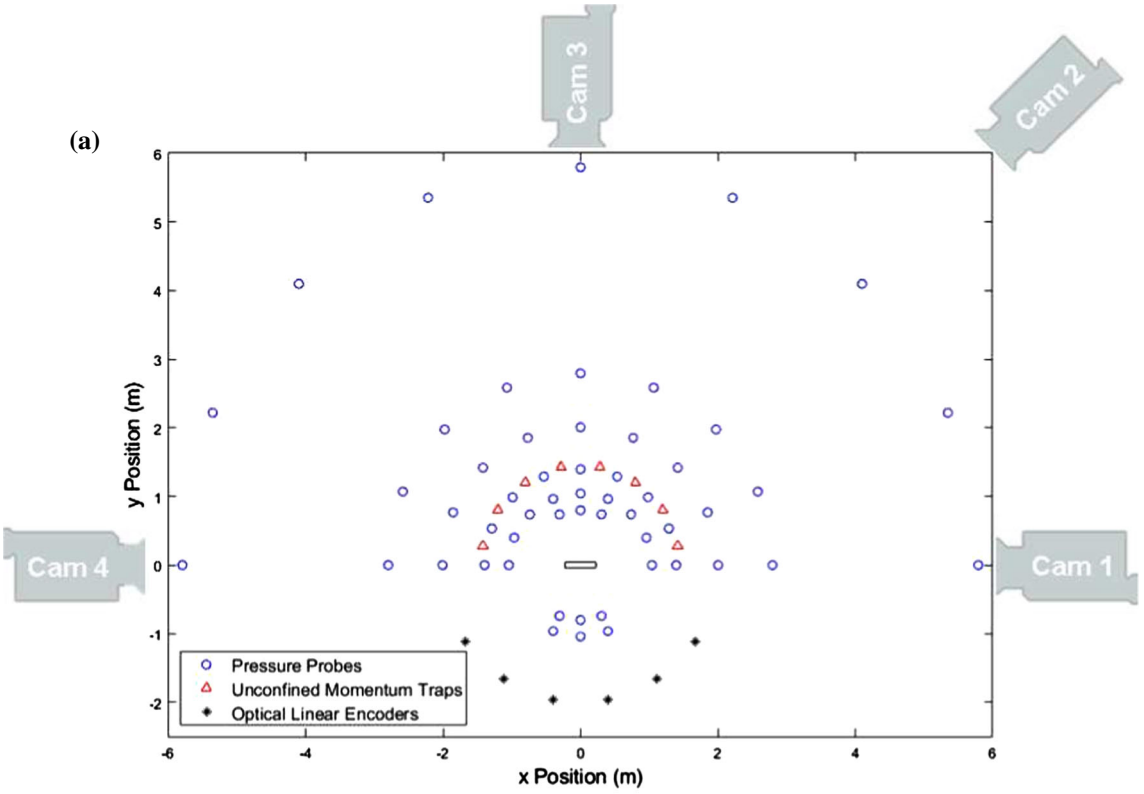

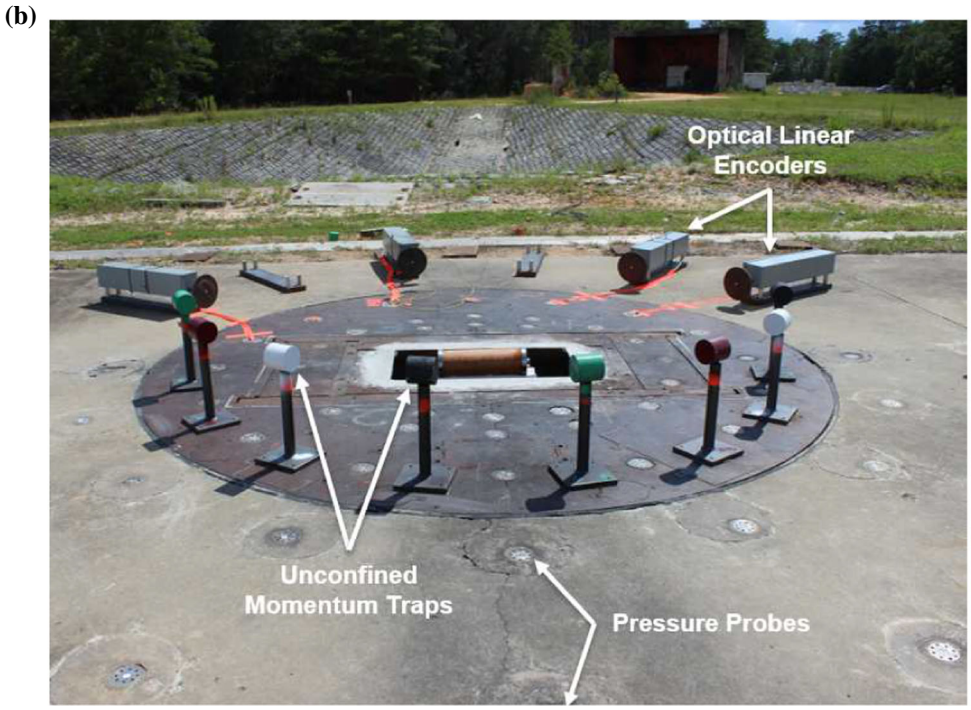

Fig. 1 AFRL blastpad outdoor testing facility. **a** Locations of the test instrumentation relative to the test charge. **b** Close-up view of a test charge suspended above the exhaust ducting; exhaust pit shown in background. To orient the reader, the photograph was taken looking at the test setup from the positive *y*-axis (similar to the view of Camera 3). The pressure probes can be seen inset into the concrete pad. The UMTs are shown in the foreground with four of the six possible OLEs shown in the background

the impact location of the UMTs was determined from the colored markings left on the concrete pad instead of impact craters in soft dirt. Between tests, old markings were crossed out to prevent erroneous readings. Also, different from Held is the necessity of placing the UMTs at an angle to the charge due to the charge being flush with the ground. As will be discussed later, this requires slightly more involved kinematics and an additional assumption. The UMTs were placed between the pressure probe radials to allow accurate reading of the primary shock. On the other side of the charge, six OLEs were mounted approximately 2 m away from the charge. However, the photodiode used in the OLE suffered from a slow discharge rate, preventing successful measurement of the explosive impulse. Therefore, the OLE results were discarded.

2.2 Test article design

The number of tests was constrained to just six by the high cost. The geometry was constrained to be cylindrical to match previous tests performed at AFRL. In addition, a tungsten shot was required for comparison to the steel particle liner charges. The experiments of Zhang et al. [12] and Frost et al. [13,14] were a significant influence on the design of the present tests. A simple, cylindrical test geometry was used, and the particle liner was restricted to a relatively small range of solid metal particles. No liquid was added to the bed (i.e., the particle liner is a dry powder bed). The tests were conducted statically instead of considering the inertial effects of a falling charge [18].

Photographs of one of the test articles are shown in Fig. 2. To ensure instabilities would arise, the literature was consulted for relevant parameters relating to the formation of instabilities. A primary measure is the ratio of the particle mass to the charge mass (M/C ratio). Other investigations show large instability waves persisting for long times [12–14,22] when the M/C is 10 or greater. To minimize the cost of the particles while ensuring the instabilities will appear, the current multiphase liner test articles were designed with a M/C ratio of 10.

Preliminary validation must be performed of the explosive model before attempting to understand the particle dispersal. Therefore, two of the six available tests were dedicated to establishing a baseline by conducting tests with no particle liner, called bare charges in this work. As a possible means to increase the sample size, it was desirable to match the explosive material, mass, and geometry of the charge to previous data collected at the AFRL blastpad. Of the available legacy data, previous Composition B tests were considered good candidates due to its ease of manufacturing, relatively high Gurney constant of approximately 2.7 km/s, and availability in the literature [23]. Composition B is machinable, allowing fine control over the charge dimensions and quality. By matching to previous legacy data, the number of baseline explosive tests was increased to four samples. Additionally, extensive effort was made to ensure the quality of the explosive charges used through close scrutiny of the charge dimensions, mass, and explosive quality.

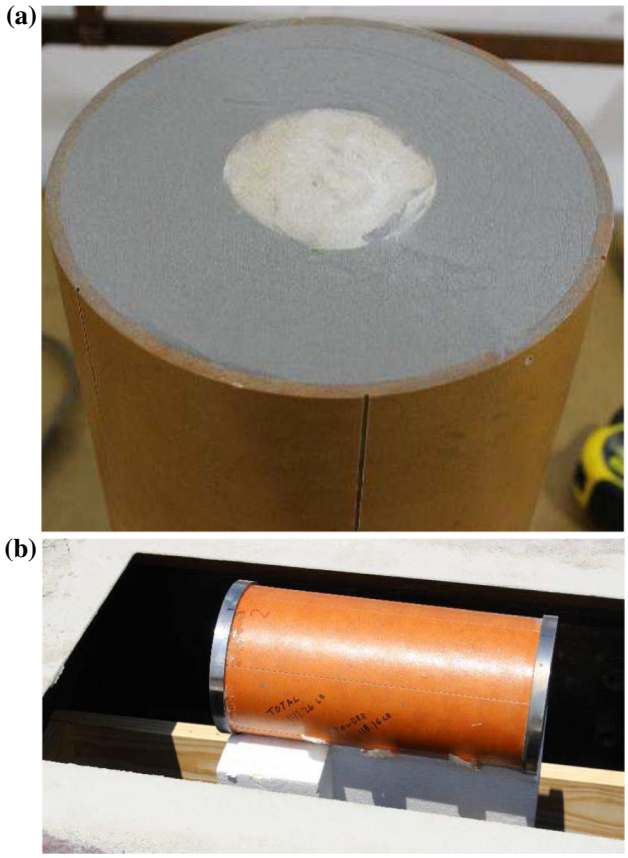

Fig. 2 Photographs of the steel liner test article. **a** Charge cross section showing thin outer wall, particles, and explosive. One of the six notches is visible in the foreground. Note there is no inner wall between particles and explosive. **b** Charge shown suspended above the exhaust tunnel on the wooden frame and Styrofoam cradle with steel end caps

Metal particles were chosen to minimize the effect of particle deformation and fragmentation while still providing access to the observed jetting instability common to explosively dispersed particles. The fingering instability for dry particle beds has been demonstrated for sand liners [22] and glass/steel liners [14]. Extensive effort was made to obtain steel particles from available vendors that are close to spherical and with a tight size range. The spherical particles were desirable to match the assumptions of spherical, monodisperse particles commonly made in multiphase simulations. In addition, the tight size range circumvents the need for time-consuming sieving of the particles, a significant concern when attempting to obtain 40 kg of test particles per shot.

From the literature, it appears that the flow is sometimes largely affected by the casing and sometimes it is not. In the first case, results published in the literature suggest that the casing fragmentation is highly correlated with the number of jets appearing when using a metal casing [18,24]. In the second case, results by Frost and collaborators have shown that changes in particle material, dry versus wet beds, etc., exhibit large differences in the character of the instability while using a glass or plastic casing [13,14]. Preferably, the experiments would operate in this latter case where the casing can be assumed to be negligible, greatly reducing the complexity and decoupling the structural and fluid dynamics. However, it remains a possibility that the casing could still be coupled to the flow. Several precautions were taken in the design to mitigate against this possibility. First, a simple, annular structure was chosen with no inner casing or struts between the pressed Composition B explosive and the particle bed. (Composition B was partly chosen as the explosive for this requirement as its relative insensitivity prevented any concern of pouring metal particles over an explosive.) Second, it was desirable to introduce notches in the casing such as in Zhang et al. [24] and Bai et al. [18]. If the observed jetting is correlated to the number and location of the notches, then it would be a strong indicator that casing fragmentation is a major player in the flow physics and that it cannot be neglected in the interpretation of the results. The inclusion of notches required that the casing not only be brittle, but had to be machinable as well. The final requirement for the casing required that tracking and observation of the casing be possible with the high-speed video cameras, a necessary condition when the diagnostics lack X-ray imaging.

The material chosen to meet these requirements was 4.76-mm-thick phenolic tubing. Estimates of the energy required to break the phenolic show the casing absorbing only a tiny fraction of the released explosive energy. First, the energy required for the casing to fail may be estimated by the integration of the stress–strain curve multiplied by the casing volume:

$$E_{\text{casing}} = \sigma_{\text{f}} \varepsilon_{\text{f}} \frac{\pi}{4} \left(D_{\text{o}}^2 - D_{\text{i}}^2 \right) L, \tag{1}$$

where σ_{f} is the failure strength and ε_{f} is the failure strain. The tensile failure strength for phenolic is approximately 610 MPa and the failure strain is 2.5% [25]. The largest casing used in the test series has an outer diameter, D_{o}, of 21.6 cm, an inner diameter, D_{i}, of 20.6 cm, and a length, L, of 44.8 cm.

Next, the released energy of the explosive may be estimated from the specific energy, e_{m}, and mass, m_{expl}, of the explosive:

$$E_{\text{expl}} = e_{\text{m}} m_{\text{expl}}, \tag{2}$$

The specific energy of Composition B is 4.95 MJ/kg [23], and the mass of the charge is 4.1 kg. The E_{expl} is approximately 20.3 MJ, while the E_{casing} is 0.23 MJ, or less than 0.2% of the explosive energy.

In addition, phenolic is easily machinable, even when considering the relatively large diameters and thin walls employed in the casing design. The brown color of the phenolic allows tracking via the high-speed cameras. As a final point on the casing design, steel end caps were used to provide sufficient structural strength to support the 44 kg of particles and explosive.

2.3 Test article and shot configuration

In summary of the previous section, six explosive tests were conducted in this series of experiments. Two tests were performed with no particle liner, so-called "bare charges". The four remaining test configurations incorporated an annular particle liner around the explosive. Two particle materials were investigated, tungsten and steel, as shown in Fig. 3. The tungsten particles were M70 Global Tungsten and provided by AFRL at significant cost savings and to meet their programmatic requirements. In addition, with the very limited number of shots it was desirable to have at least three repeated shots for one configuration. Three steel shots were pursued, while only tungsten shot was completed. The M70 tungsten particles are reported by the manufacturer to have been sieved through a US size 40 (425 μm) sieve with an average particle size of between 15 and 40 μm. The steel particles (410 alloy) were obtained from Sandvik Osprey and reported by the manufacturer to have been sieved between 75 and 125 μm. Scanning electron microscope (SEM) analysis of the steel particles yields an average diameter of 115 μm. Table 1 contains a summary of the test configurations including the volume fraction, ϕ, and M/C for the particle liner tests. For the particle liner tests, 4.76-mm-thick phenolic tubing was used as a casing. In three of the particle liner tests, six notches traveling the long axis of the test article were machined into the casing (Fig. 2b). The notches serve to weaken the case structure at predetermined locations and are 2.54 mm wide and 1.27 mm deep (approximately 25% of the wall thickness). The six notches were equally distributed around the circumference of the casing, 60° apart.

Photographs of the explosive charge with a particle liner are presented in Fig. 2. The explosive train consisted of a Teledyne RISI RP-80 detonator, a 25.4-mm-diameter by 25.4-mm-length A5 booster pellet (23 g), and 4.1 kg of Composition B. The Composition B charges were nominally 8.19 cm in diameter and 44.7 cm in length. The explosive is end initiated and burns in the positive x-axis direction. The explosive casing was supported by two lipped 5.2-mm-thick steel caps. Wooden chucks are used to center the explosive with the phenolic casing and then removed as the particles

Table 1 Shot configuration for the six test articles

Shot	Particle liner	Mass of particles (kg)	M/C	ϕ	Notched
1	–	–	–	–	–
2	–	–	–	–	–
3	Tungsten	40.86	10.0	0.41	Y
4	Steel	53.22	13.0	0.55	Y
5	Steel	53.60	13.1	0.56	Y
6	Steel	53.84	13.1	0.56	N

Note the large difference in volume fraction between the tungsten and steel particle liners. Uncertainty of the tabulated values is: ± 0.01 kg for the mass of particles, ± 0.1 for M/C, and ± 0.01 for ϕ

sufficiently pack around the explosive to hold it in place. The steel end caps are then epoxied to the casing.

The charges were designed to achieve a M/C of 10 with an assumed ϕ of 40%. The assumed 40% arose from preliminary small-scale tests measuring the volume fraction of the steel and tungsten particles. Based on this assumed volume fraction, the casing for the tungsten particles was 15.5 cm in diameter and the casing for the steel particles was 21.6 cm. These casing diameters give a tungsten particle liner that is 3.15 cm thick and a steel particle liner that is 6.17 cm thick. The 40% volume fraction proved an accurate assumption for the tungsten particles while the steel packed closer to a 60% volume fraction. This discrepancy led to a departure in the steel particle liner M/C. The difference in the close-packing volume fraction between the tungsten and steel shots was perhaps due to the fact that the steel particles were nearly spherical, while the tungsten particles were not (see Fig. 3). Approximately 41 kg of tungsten particles were used, giving a M/C of 10. Conversely, approximately 53 kg of steel particles were used in each steel test to give a M/C of 13.

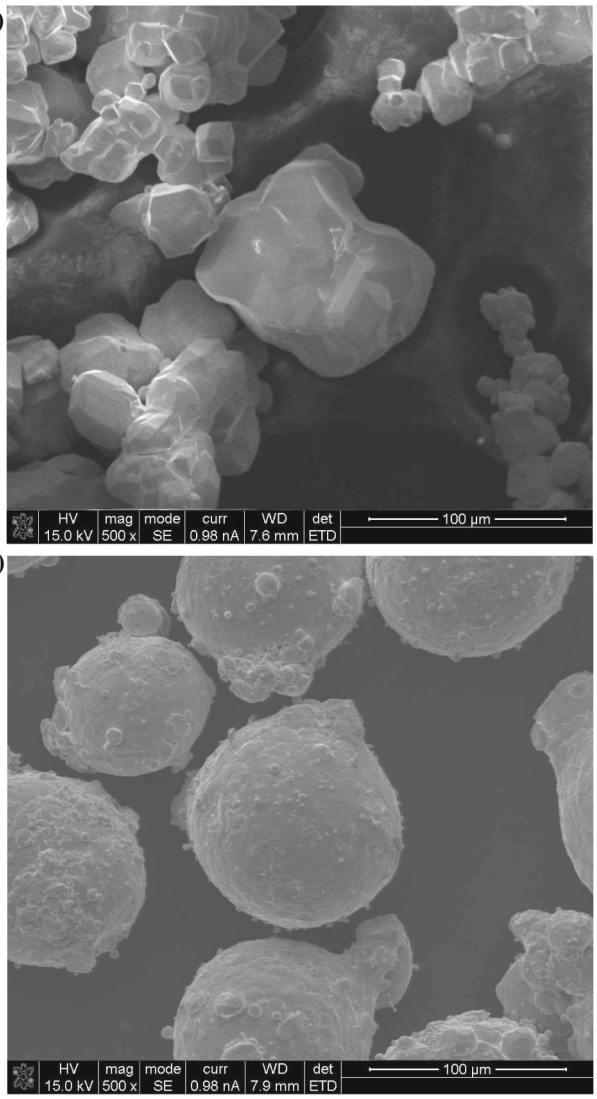

Fig. 3 Representative particles used in the particle liner shots. **a** Tungsten particles obtained from Global Tungsten. **b** Steel particles obtained from Sandvik Osprey

3 Input uncertainty quantification

This section will detail uncertainty quantification of the experimental inputs. Measurement of the explosive charges, the particle size distribution, particle density, and volume fraction variation will be presented. Our primary focus is on the steel particles, and therefore, the tungsten particles were not characterized as rigorously as the steel particles.

3.1 Explosive length, diameter, and density

The six Composition B charges were manufactured at the High Explosives Research and Development Facility (HERD) located on Eglin AFB. The HERD measured the diameter and length of the explosive after manufacture, with several diameter measurements along the length to ensure a consistent diameter. The results shown in Table 2 demonstrate the low degree of uncertainty in the charge geometry. The measured diameters and length show less than 0.1% uncertainty both between charges and within various diameters measured along the length of the same charge.

Table 2 Measurements in millimeters of charge dimensions to assess geometric uncertainty along the length of the charge

Charge	Dia. (mm)					Length (mm)	Mass (g)	Density (g/cm^3)	% TMD
	Bottom	1/4	Mid	3/4	Top				
1	81.92	81.94	81.92	82.04	82.04	447.7	4100	1.735	99.6
2	81.86	81.86	81.89	81.94	81.94	447.8	4086	1.732	99.4
3	81.89	81.92	81.92	81.89	81.92	447.7	4100	1.738	99.8
4	81.86	81.86	81.94	81.94	81.94	447.4	4096	1.737	99.7
5	81.92	81.92	81.92	81.94	81.94	447.1	4108	1.743	100.0
6	82.04	82.04	81.89	81.92	81.89	447.8	4109	1.740	99.9
μ	81.92	81.92	81.91	81.94	81.94	447.6	4100	1.738	99.7
σ	0.07	0.07	0.02	0.05	0.05	0.2	8	0.004	0.2

Calculated charge density with comparison to percent theoretical maximum density (% TMD). The TMD used for Composition B was 1.742 g/cm^3

Table 2 also presents the explosive density, a key simulation parameter, and its relation to the maximum theoretical density as a percentage (% TMD). The length and diameter of the explosive were used to estimate the volume of the charge assuming a perfect cylinder. The mass of each charge was measured using a mass balance, demonstrating a 0.2% uncertainty. The density for each individual charge was estimated and shown to contain less than 0.3% uncertainty. The TMD used is 1.742 g/cm^3 and was obtained from Dobratz and Crawford [23].

The charges were examined externally to ensure no chips or gouges were present. In addition, each explosive charge was X-ray tested to ensure the absence of flaws or voids, as such inhomogeneities would be challenging to modeling and simulation of the detonation process.

3.2 Particle size distribution

Particles were reported by Sandvik Osprey as sieved between 75 and 125 μm. The particle size distribution of the steel particles was quantified from a series of 25 SEM images. Images were segmented with a global threshold manually determined from the image histogram. The equivalent diameter, d_e, of the particles was obtained from the following relation:

$$d_e = C\sqrt{\frac{4A}{\pi}}, \tag{3}$$

where A is the area of the segmented pixels for each particle and C is the calibration constant obtained from the SEM image. Figure 4 contains an example image and the accompanying segmentation results with the boundaries of the segmented particles shown in red and overlayed on the original image. Particles touching the image boundary are rejected.

Two distributions of particles were apparent during the post-processing, the small particle sizes (1–20 μm) and the large particle sizes (60–240 μm). The small particle sizes

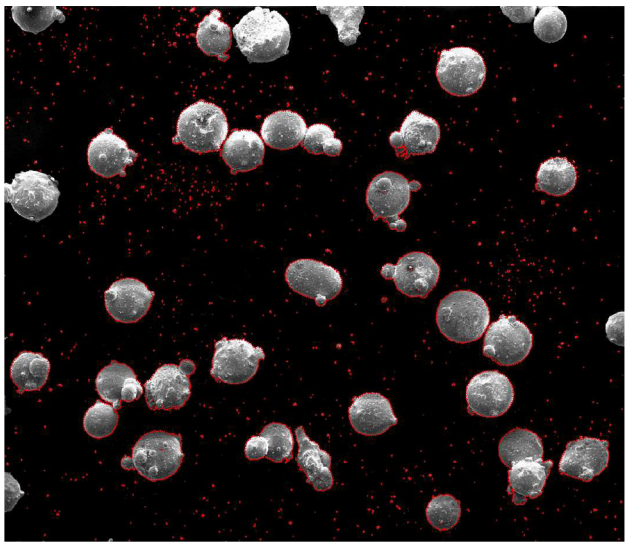

Fig. 4 Sample of SEM image used to obtain the particle size distribution showing both large and small particles present. Traces (red) indicate the selected boundaries of the particles. Particles touching the image boundary are rejected

appear to be an artifact of the manufacturing process. The large particles have many small nodules on their surface. It is postulated that subsequent handling after sieving constantly breaks the small nodules from the surface of the large particles and gives rise to their presence in the sample. Note that even with the large number of small particles present in the sample, the majority of the small particles remain attached to the large particles as nodules. Particles larger than the stated sieve size arise due to aggregates or elongated particles that appear more ellipsoidal than spherical. Particle size results are presented as histograms in Fig. 5 and summary statistics in Table 3. Note that the mean of the large particles, 115 μm, is on the high side of the reported size range.

As shown in Fig. 5, both small and large particle sizes appear to follow a log-normal distribution. Fitting of the small and large particle distributions with 16 candidate distributions showed the log-normal distribution fit with minimum

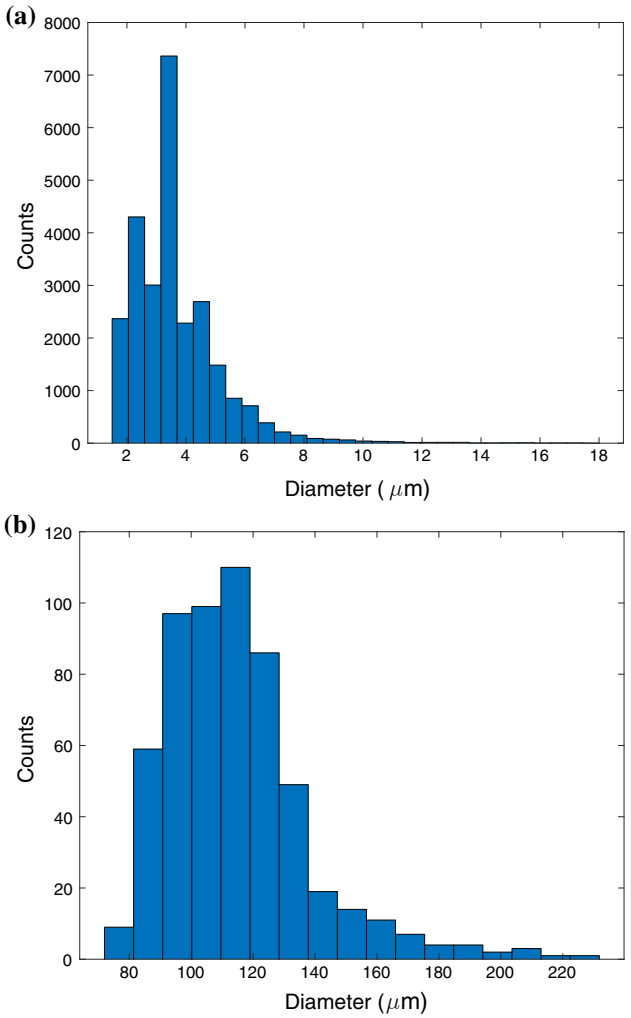

Fig. 5 Histograms of the measured particle diameters. **a** Small particle sizes ($< 60\,\mu$m). **b** Large particle sizes ($> 60\,\mu$m)

Table 3 Summary statistics of the equivalent particle diameter for the two particle size ranges

	Sample size	μ (μm)	σ (μm)
Small particles	26,228	3.6	1.5
Large particles	575	115	23

negative log-likelihood. However, a variety of statistical tests (Anderson–Darling, Lilliefors, χ^2) rejected the log-normal fit and several other likely candidates (log-logistic, Weibull, Generalized Extreme Value). Figure 6 shows the probability plot of the particle diameters against the log-normal fit and reveals that the tails depart from the assumed fit. In addition, the very small particles suffer from the resolution of the image and binning of the particle sizes becomes apparent on the probability plot. Nevertheless, from the measurements it can be concluded that the small particles have much less than 1% of the mass of the large particles and therefore are

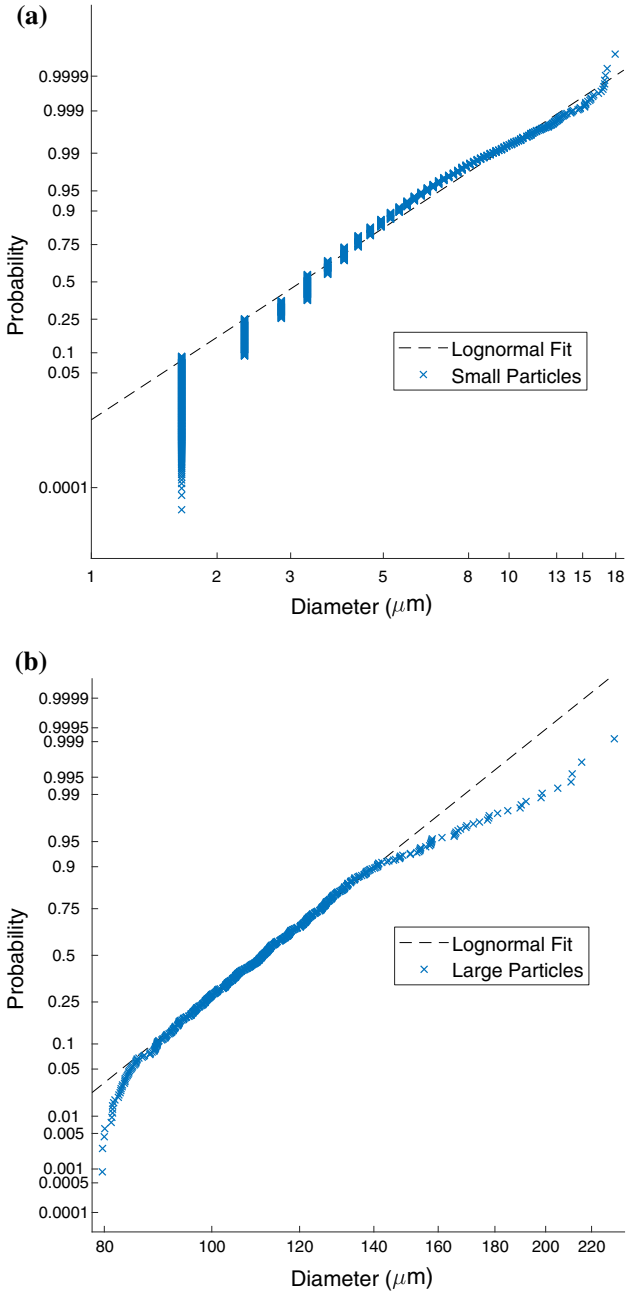

Fig. 6 Probability plot of the empirical data compared to the log-normal distribution. **a** Small particle sizes ($< 60\,\mu$m). **b** Large particle sizes ($> 60\,\mu$m)

not expected to change the behavior of the blast wave (initial shock) or the evolution of the main particle front.

3.3 Particle density

The steel particles (410 alloy) have a manufacturer-reported density of 7.73 g/cm^3. The particle density was derived from a fluid displacement method to independently determine the density. In this method, a sample of particles was first measured with a mass balance and then their volume determined

Table 4 Casing dimensions (in cm) as measured by a tape measure

Shot	Inner diameter	Outer diameter	Length
3	14.7	15.6	44.7
4	20.6	21.6	44.8
5	20.6	21.5	44.9
6	20.7	21.6	44.8

The measurement uncertainty is approximately ± 0.1 cm

from a helium gas pycnometer (Quantachrome UltraPyc 1000 Gas Pycnometer). The advantage of using helium as a working fluid lies in the ability of the helium gas to penetrate into most pores on the particle, giving a more accurate measure of the true particle density. A sample was taken from the same batch used in the experiments, and the mass was measured to be 111.6748 ± 0.0001 g. The large mass of particles was necessary because a significant volume of the particles was required to achieve accuracy from the pycnometer. In addition, the volume of the particles was measured through a series of 12 runs to reduce the sampling uncertainty of the pycnometer. The volume of the particles was measured to be $14.59 \pm 0.02\,\text{cm}^3$ with a resulting density of $7.655 \pm 0.009\,\text{g/cm}^3$. The density of the particles has a small, but significant, difference from the manufacturer-reported density.

3.4 Casing dimensions

Casing dimensions were measured with a tape measure, with a resulting measurement uncertainty of approximately ± 0.1 cm. The casing dimensions presented in Table 4 were combined with the explosive charge geometry, particle density, and measured mass of particles to calculate the global volume fraction presented in Table 1.

3.5 Local particle volume fraction

Moderately spherical particles poured into a bed with a minimum of shaking and vibration may commonly be expected to pack with a volume fraction between 0.59 and 0.63 [26]. While the average volume fraction may be reasonably estimated by bulk measurements, it is of some interest to pursue local measurements of the volume fraction to estimate its variation within the bed. Simulation efforts such as those pursued by Annamalai et al. [27] have shown that the large-scale instabilities present in the explosive dispersal of particles may be excited by perturbation of the initial volume fraction of the bed. Experimental examination of the local volume fraction aims to determine what level of variation is preexisting in a randomly packed bed.

A computed tomography (CT) scan of a bed of steel particles is shown in Fig. 7. In order to achieve a resolution that may accurately reconstruct the particles, a bed approximately 9 mm in diameter is the largest sample bed that could be examined. As the bed diameter is increased, the resolution of the CT scan drops. With a 9-mm-diameter bed, the voxel resolution was $10.5\,\mu$m, giving approximately 10 voxels across the average particle diameter. While being significantly smaller than the bed in the explosive experiments, the bed still contains $O(10^6)$ particles. The steel particles used are from the same batch used in the explosive experiments. Three sample beds were prepared. Bulk measurements of the steel samples are presented in Table 5. The volume of each sample was $5 \pm 0.1\,\text{cm}^3$. The mass of the bed was measured within ± 0.0001 g. To estimate the mean volume fraction, ϕ, of each sample, the following relation was used:

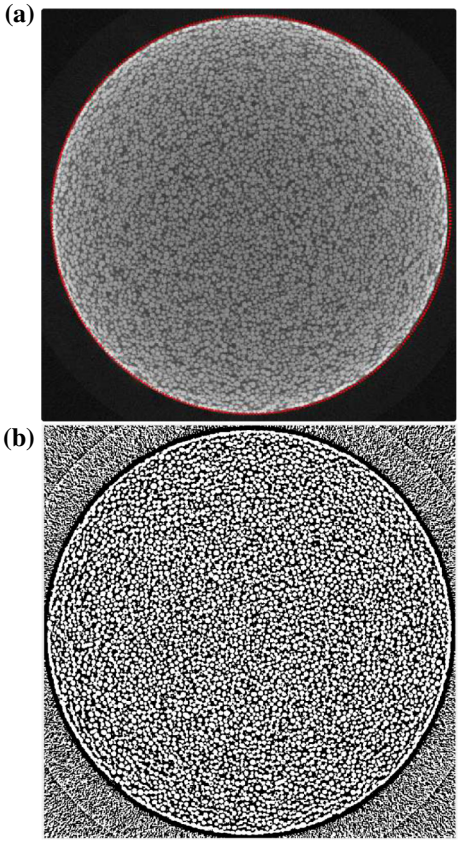

Fig. 7 Example images of the local volume fraction processing procedure. **a** Example slice of the particle bed. The dashed boundary (red circle) was used to segment the particle bed from the background. **b** Accompanying segmentation results using the local threshold method. Results outside the black circle were ignored

$$\phi = \frac{\rho_\text{b}}{\rho_\text{st}}, \tag{4}$$

where ρ_b is the bulk density and ρ_st is the steel density obtained from the measurements presented in the previous section, $7.655 \pm 0.009\,\text{g/cm}^3$. The mean volume fraction was

Table 5 Bulk measurements of the steel sample used for the CT scan

Sample	Mass (g)	Bulk density (g/cm^3)	ϕ
1	21.7238	4.34	0.57
2	22.1607	4.43	0.58
3	22.2455	4.45	0.58
μ	22.04	4.41	0.58
σ	0.28	0.06	0.01

Volume of each sample is $5 \pm 0.1\,\text{cm}^3$. Steel density was obtained from the measurements presented in the previous section, $7.655 \pm 0.009\,\text{g/cm}^3$

estimated as 0.58 ± 0.01. Note that this value is consistent with the volume fraction of the steel beds in the explosive experiments.

To measure the local volume fraction, the CT scan was exported as a series of slices over a total bed height of 18–20 mm. An example is shown in Fig. 7a. The particles were segmented from the background using the threshold generated by the Otsu method [28] on a 15×15 pixel subregion. A local thresholding method was required due to a gradient within the slice. The gradient is an artifact of the reconstruction method, commonly referred to as "beam hardening" and spuriously shows material on the outside of the region of interest to be less dense than the interior [29]. Use of a global threshold results in a bed with smaller particles on the interior of the bed and merging of individual particles on the exterior of the bed. Figure 7b shows that the local threshold method largely corrects for this gradient as the particles appear of approximately constant size across the bed.

While the results were not very sensitive to the size of the pixel neighborhood chosen, degraded performance was observed if the neighborhood was made too large or too small. When decreased to a 5×5 neighborhood, the segmentation process began to show holes appearing within individual particles. When increased to a 50×50 neighborhood, similar issues as that shown by the global threshold returned, such as particles merging with their neighbors.

The volume fraction is equal to the areal fraction [30]. Therefore, to calculate the volume fraction of the i-th slice, the thresholded pixels in the slice, $A_{\text{th},i}$, were divided by the total number of pixels within the particle bed, A_{tot}:

$$\phi_i = \frac{A_{\text{th},i}}{A_{\text{tot}}}, \tag{5}$$

Results for the local volume fraction are shown in Fig. 8. The reader will note that ϕ_i does not begin at zero. The origin of the measurement was set where the first particle became visible in a slice. However, the top of the particle bed was not completely flat and did not take up the entirety of the slice. To maintain consistency, these slices were removed, beginning the sample once the particles completely filled

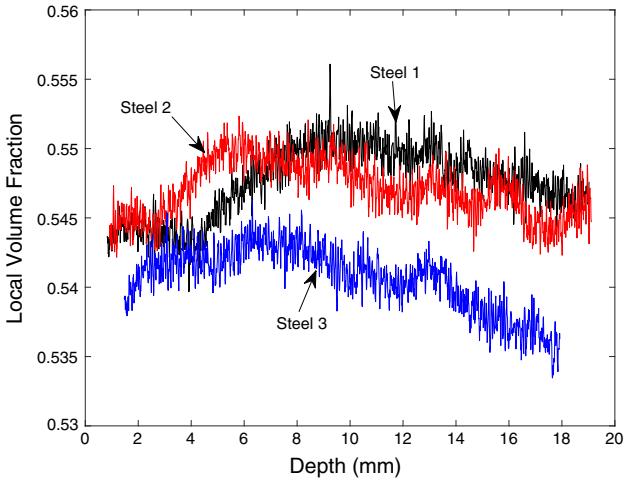

Fig. 8 Local volume fraction determined at each slice

Table 6 The mean and standard deviation of the local volume fraction, ϕ_i, obtained from CT scans of the three sample beds

Sample	n	μ_{ϕ_i}	σ_{ϕ_i}
1	1722	0.548	0.003
2	1722	0.547	0.002
3	1557	0.541	0.002
Aggregate	5001	0.545	0.004

The sample size, n, is shown for reference. Aggregate refers to the combination of all three samples

the region of interest. In all three samples, the local volume fraction exhibits an increase followed by a steady decline after moving 6–10 mm in the bed, exhibiting the presence of a small but noticeable gradient of the volume fraction. However, the local volume fraction variation appears to be outweighed by the sample-to-sample variation.

The local volume fraction results are lower than the 0.58 ± 0.01 volume fraction predicted by the bulk measurement. (The means are separated by more than three standard deviations of the two distributions.) It is likely that insufficient resolution to resolve the small particles and surface nodules is the culprit. While the small nodules are a very small fraction of the total mass, the nodules serve to separate the particles preventing their packing while being too small to be resolved by the CT scanner. Regardless, the measurement can be used to quantify the local volume fraction variation through statistical measures as this variation can still be used to seed simulations with a "realistic" volume fraction perturbation. Table 6 contains summary statistics of the three samples and the aggregate, which is the combination of the three samples. The results show the variation is small even for the aggregate, showing less than 0.1% variation in ϕ_i.

Combining the three samples, the areal fraction results are plotted as a histogram, as shown in Fig. 9a. Fitting ϕ_i with

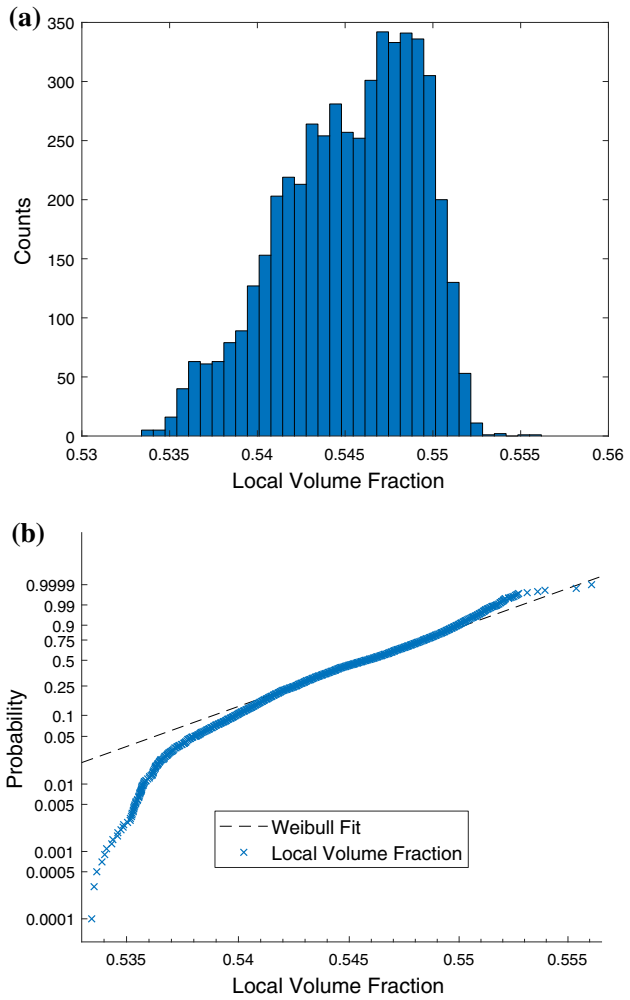

Fig. 9 Statistical plots of the local volume fraction. **a** Aggregate histogram of the local volume fraction from three sample beds. **b** The Weibull distribution was the most likely candidate fit but shows departure at the tails of the distribution

16 candidate distributions showed the Weibull distribution fit with minimum negative log-likelihood. However, a variety of statistical tests such Anderson–Darling, Lilliefors', and χ^2 all rejected the Weibull fit. Figure 9b shows the probability plot of ϕ_i against the Weibull fit and reveals that the tails depart from the assumed fit.

3.6 Ambient conditions

Ambient temperature and pressure were not directly measured at the AFRL blastpad. Instead, pressure and temperature bounds were obtained from a weather archival Web site, Weather Underground, for the reported test times and are tabulated in Table 7. Three surrounding weather stations issue hourly reports of the temperature and pressure. To build the ambient conditions interval, the two weather reports closest in time were taken from each station. The maximum and minimum values from the six available values form the bounds for each variable. For convenience, the bounds for the temperature and pressure for all six shots have been compiled under the "All shots" entry.

Table 7 Ambient temperature and pressure bounds for the AFRL blastpad tests

Shot	Time stamp	Press. (kPa)	Temp. (°C)
1	7/19/2017, 10:46	[102.10 102.13]	[28.5 32.0]
2	7/19/2017, 13:35	[101.96 102.07]	[30.8 33.9]
3	7/19/2017, 16:40	[101.76 101.90]	[30.7 33.9]
4	7/20/2017, 11:10	[101.93 102.00]	[32.1 33.9]
5	7/20/2017, 15:29	[101.63 101.76]	[26.0 34.4]
6	7/28/2017, 13:03	[101.29 101.39]	[33.2 35.0]
All shots	7/19–7/28	[101.29 102.13]	[26.0 35.0]

Table 8 Summary table of the uncertain inputs quantified for the blastpad tests

Parameter	Value	Method
Explosive diameter	81.93 ± 0.03 mm	Mfr. Data
Explosive length	447.6 ± 0.2 mm	Mfr. Data
Explosive density	1.738 ± 0.004 g/cm^3	Derived quantity
Particle diameter	115 ± 23 μm	SEM analysis
Particle density	7.655 ± 0.009 g/cm^3	Gas pycnometer
Casing inner dia.	20.6 ± 0.1 cm	Tape measure
Global vol. fraction	0.56 ± 0.01	Derived quantity
Local vol. fraction	0.545 ± 0.004	CT scan
Ambient press.	[101.29 102.13] kPa	Archival weather
Ambient temp.	[26.0 35.0] °C	Archival weather

3.7 Summary of uncertain inputs

The results from the previous five sections are summarized in Table 8. Quantification of the variability of each value is presented as $\mu \pm \sigma$ (except in the case of the ambient conditions) and is listed with the method used to obtain each value. The reader is referred to the pertinent subsections within the section for further information.

4 Results

This section will present results from the various diagnostics present in the explosive tests. First, the pressure probes will be processed for shock time of arrival and peak pressure. Second, the unconfined momentum traps will be processed for total impulse imparted by the fluid and particles. Third, the high-speed cameras will be processed to extract the shock time of arrival and contact/particle front positions. Note the error bars in the following results represent $\pm 1\sigma$.

4.1 Pressure probe results

The pressure histories obtained from the 54 inground pressure probes were processed to recover the peak pressure (P_{peak}) and the shock time of arrival (ToA). The probes positions within the concrete pad were confirmed by a tape measure, and their positions were found to be within 2% of nominal (see Fig. 1a). The P_{peak} is defined as the first large peak encountered by the probe. Some of the pressure histories were subject to large fluctuations due to noise or debris impacting the pressure transducer and have been manually corrected to ensure erroneous peaks were not selected. P_{peak} results are reported in gauge pressure. The ToA was determined as the time when the pressure reaches 50% of the P_{peak}, as shown in (6). An example pressure trace with P_{peak} and ToA identified is shown in Fig. 10b.

$$\text{ToA} = t(P = 0.5P_{\text{peak}}) - t_0, \tag{6}$$

The initial time for the pressure probes is aligned with the detonator initiation. To accomplish this task, the trigger to detonator initiation delay, t_0, was determined from the Pearson probe wrapped around the trigger line (Fig. 10a). The Pearson probe results show a sudden drop in current derivative as the exploding bridgewire within the detonator activates. The sharpness of the drop allows determination of t_0 within $\pm 2\,\mu$s.

Due to the large number of transducers, a P_{peak} field can be constructed, as shown in Fig. 11. Linear interpolation was used between the pressure transducers. The bare charge shows local maxima at the 0°, 90°, and 180° directions, as is typical for a bare cylindrical charge [20,21]. A pronounced local minimum is visible at the 45° line. In contrast, the tungsten and steel liner shots greatly reduce the P_{peak} over the entire measured pressure field and smooth out the pressure field such that local minima and maxima are much less pronounced. In addition, the 90° line no longer experiences a local maximum but changes to a local minimum for the steel shots. Local maxima can still be observed at the 0° and 180° due to the significantly smaller amount of metal present in the end caps and the direction of the burn down the length of the charge.

As mentioned previously, the charge geometry was designed to match legacy bare charge tests. The legacy tests were performed in October 2010 and February 2011, leaving a 6-year gap between the old and new tests. If the new results do not show any indication of bias, there is reasonable confidence that the legacy tests are subject only to random error and the tests may be included in the validation of the explosive model. Matching the bare charge results for the ToA and P_{peak} is basic checks for the explosive modeling. The results for ToA and P_{peak} are presented on the 90° radial for ease of comparison, but similar conclusions may be drawn

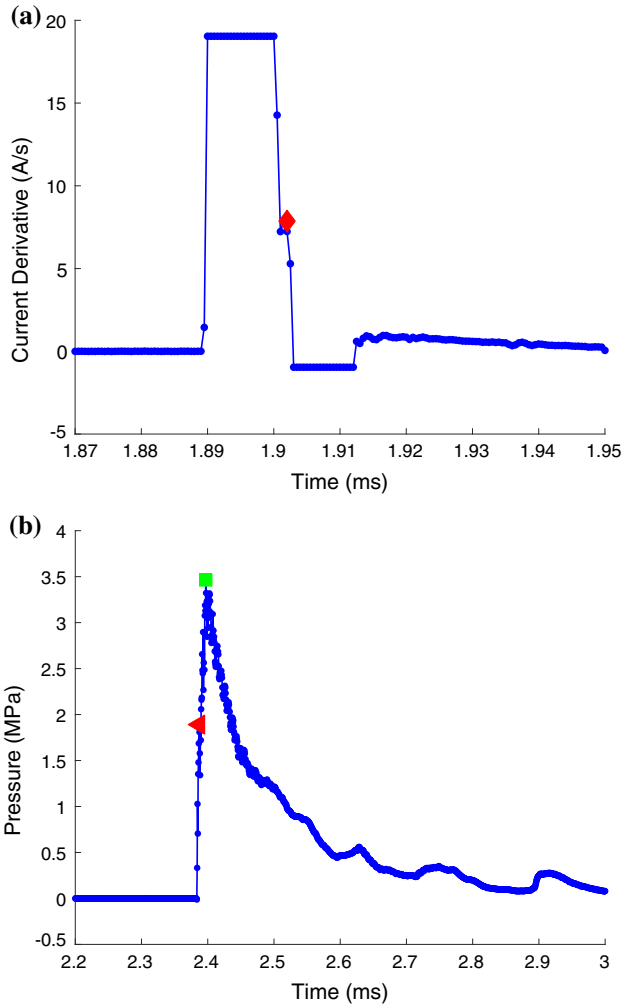

Fig. 10 Example results for detonator delay, peak pressure, and shock time of arrival. **a** Pearson probe results showing the sudden drop in current when the exploding bridgewire within the detonator activates. The t_0 shown is $1902 \pm 2\,\mu$s (red diamond). **b** Sample pressure history showing the selected peak pressure (green square) and time when the pressure reaches 50% of the peak (red triangle). The times in the pressure history have not yet been corrected by the detonator delay to demonstrate how the metrics are extracted from the raw data

from any chosen radial. Figure 12 presents the experimental results along the 90° for the bare charge with the legacy data, where close examination of the data shows no discernible pattern in the results to indicate a bias between the old and new data. The sample size for the bare charge may therefore be increased to the modest sample size of four instead of two.

The experimental results provide some evidence that the casing does not affect the ToA or P_{peak}, as shown for the three repeated steel shots in Fig. 13. Again, the results are presented on the 90°. The results for ToA exhibit very little spread, while the P_{peak} plot shows a greater variation. More importantly, the spread appears to be random in nature, with no discernible pattern based on case notching. Weakening a casing that was designed to require minimal energy

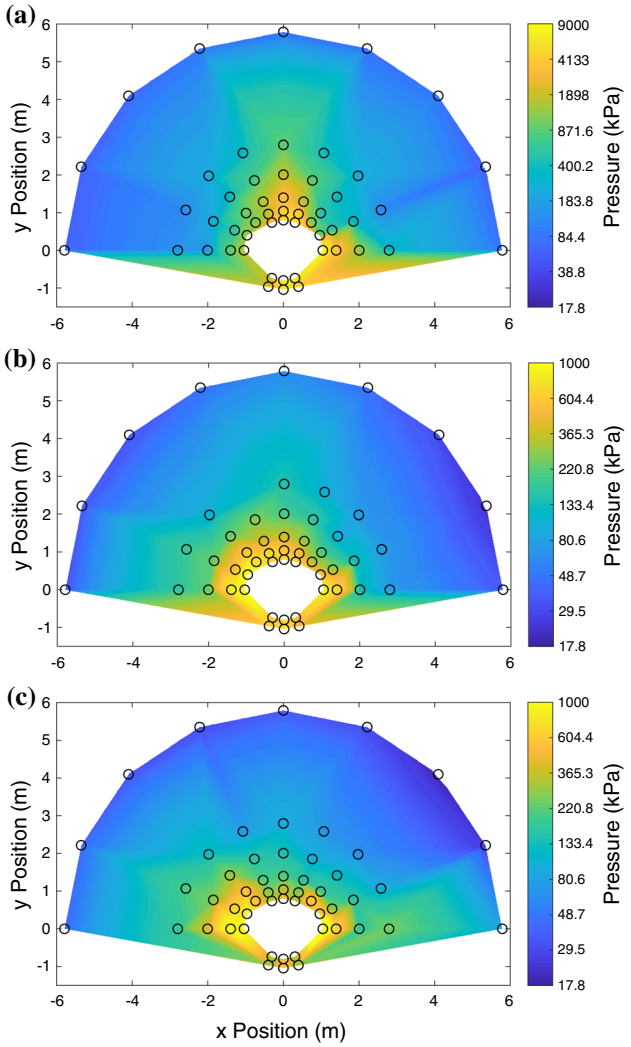

Fig. 11 Interpolated peak pressure fields between the pressure probes (shown as black circles). Repeated tests exhibit similar behavior as those shown here. **a** P_{peak} field of the bare charge (Shot 1) showing local maxima at the 0° and 90° lines. **b** P_{peak} field of the tungsten liner (Shot 3) showing a local minimum at the 45° line. **c** P_{peak} field of the steel liner (Shot 4) showing a local minimum at the 90° lines. The color bar in figures **b**, **c** has been reduced to show the details present in the pressure fields

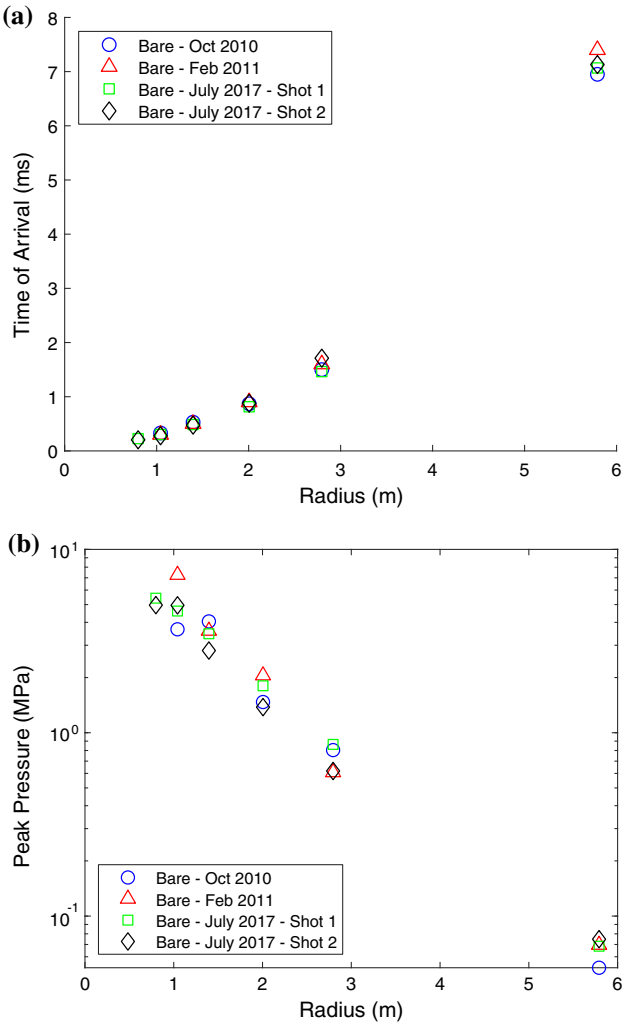

Fig. 12 Consistency of legacy data with new results. The legacy tests were performed in October 2010 and February 2011. The current tests were performed in July 2017. Data are presented on the 90° for the **a** ToA and **b** P_{peak}. No discernible bias between the legacy and current data is present suggesting the results may be included in the explosive validation

to fragment does not appear to effect the shock ToA or P_{peak}.

The above analysis shows favorable evidence for the inclusion of the legacy data and disregard of case notching. Combining the data, the results may be averaged and error bars constructed, as shown in Fig. 14. The bare charge configuration now contains a sample size of four, the tungsten liner configuration is still a single sample, and the steel liner configuration now contains three samples. The ToA for the bare charge is especially vital to validation as the image analysis was unable to recover the experimental shock location.

4.2 Unconfined momentum traps

The unconfined momentum traps (UMTs) give the impulse imparted by the particles and fluid acting together. The imparted impulse is calculate with:

$$I = m_1 V_1 - m_0 V_0, \tag{7}$$

where m is the mass of the UMT and V is the velocity. State 0 is the initial, at rest state while state 1 is the state immediately after the object has been impulsively acted upon. The UMTs were weighed before and after each test, and masses were constant within the uncertainty of the measurement.

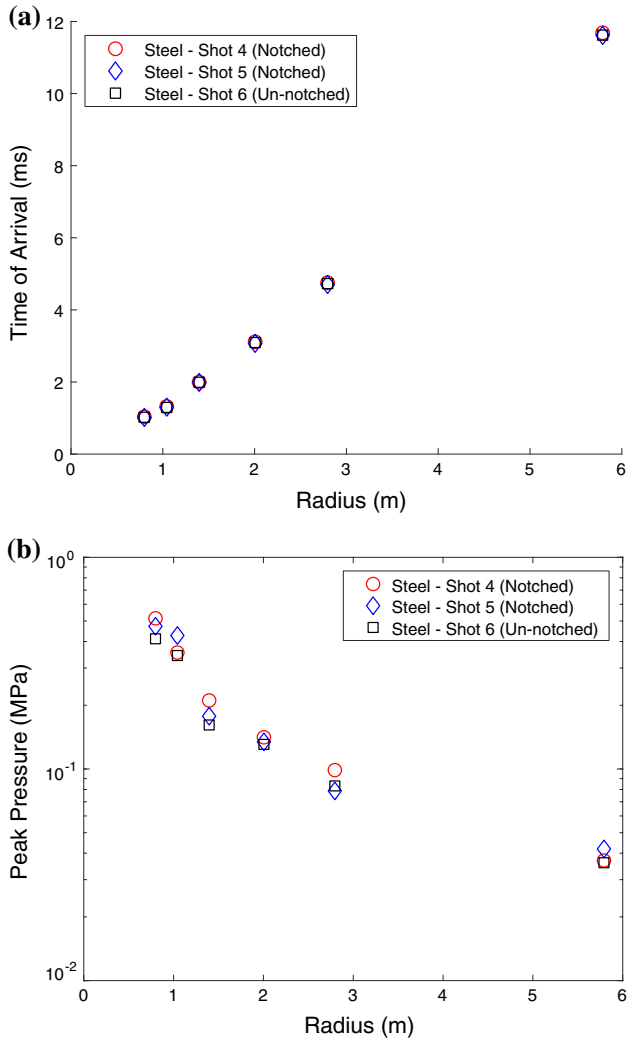

Fig. 13 Effect of case notching on the **a** ToA and **b** P_{peak}, presented on the 90°. The notching shows no discernible difference in the pressure results, allowing the steel tests to be treated as three repeated tests

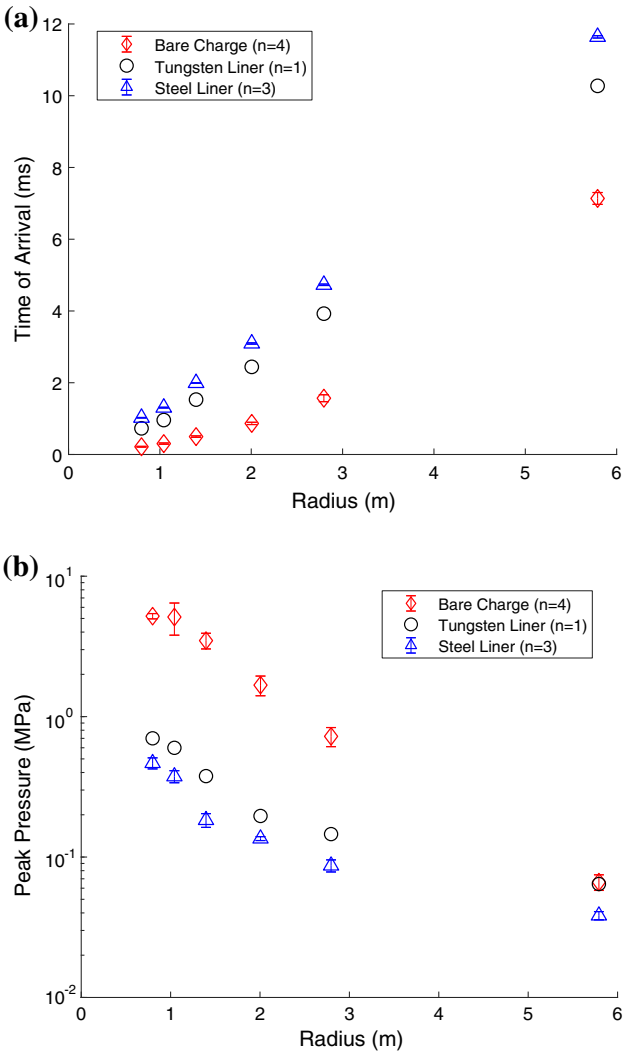

Fig. 14 Average and standard deviation of the pressure probe results for **a** ToA and **b** P_{peak}. Bare charge ($n = 4$) and steel liner ($n = 3$) configurations are averages, while the tungsten is a single sample

The mass of each UMT is 2.230 ± 0.003 kg. Normalizing the impulse by the loaded area, A, the equation becomes:

$$I/A = \frac{mV_1}{A}, \tag{8}$$

As mentioned in the experimental setup, the UMTs are a passive diagnostic, consisting of eight, 10.2-cm by 10.2-cm aluminum cylinders placed around the charge and thrown by the blast. The UMTs are numbered from 1 to 8 with 1 being the closest to the negative x-axis and then proceeding in a clockwise manner, spaced 22.5° apart. The impact locations of the UMTs are recorded in Fig. 15a in x–y coordinates. UMT impact locations were recorded with a tape measure, giving approximately 1% error. Note the qualitative agreement with the bare charge pressure probe results. Local maxima are recorded in the UMTs near the 0°, 90°, and 180°. The local minimum near the 45° results in some of the UMTs having an almost zero throw distance. However, the difference here is that the UMTs are being pushed by both the particles and the fluid whereas the probes record just the gas phase.

To convert the UMTs throw distance, x_{dist}, to impulse per unit area, I/A, the UMTs are considered ballistic projectiles. The inertia of the heavy UMTs causes them to move at time scales much slower than the explosive event, such that their momentum is impulsively applied. Simple kinematics may be employed such as used by Held [20,21] to find the launch velocity, V_1. Drag may be included in the determination of the launch velocity of the UMT, and the resulting nonlinear ODE can be solved. But, the resulting launch velocity changes by less than 0.5% and so the drag effect may be safely neglected from consideration. However, because the

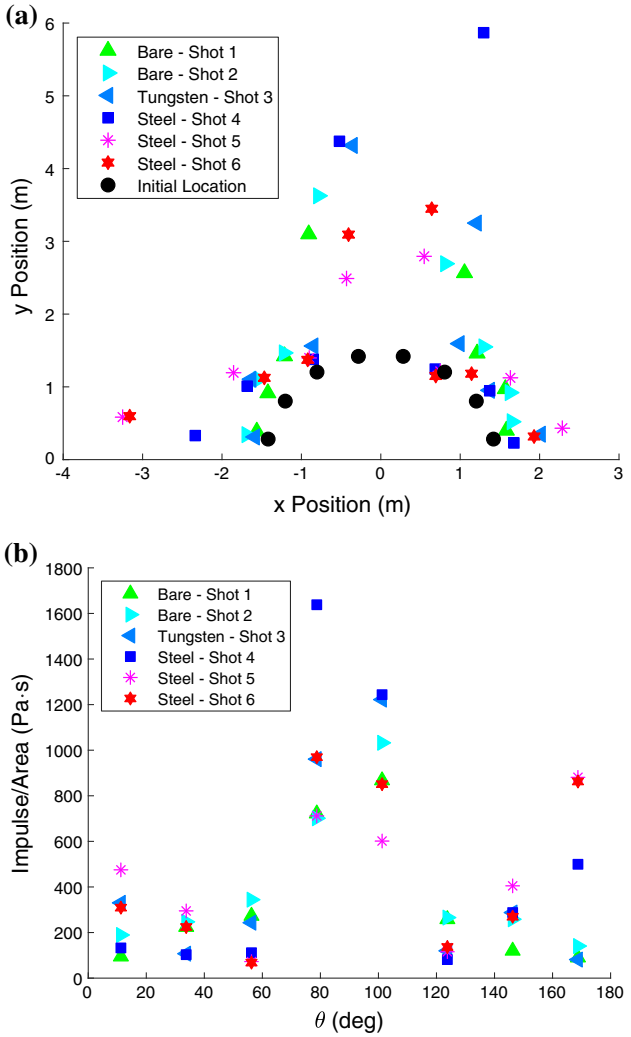

Fig. 15 UMT impact locations and derived impulse results. Error bars are occluded by the markers. **a** Recorded impact locations of the UMTs on the blastpad for each test. Impact locations have approximately 1% error. **b** UMT impulse results obtained from kinematic relations. Propagated error in I/A is approximately 1%. θ has an uncertainty of approximately $\pm 0.5°$

UMTs are at an angle with the charge, the kinematic equation is now a function of both x_{dist} and the angle of the launch velocity, α, as shown below:

$$x_{\text{dist}} = V_1 \cos(\alpha) \left[\frac{V_1 \sin(\alpha) + \sqrt{V_1^2 \sin^2(\alpha) + 2gh}}{g} \right], \tag{9}$$

where h is the initial height of the UMTs on their stands, 45.7 cm, and g is the gravity constant. To solve the equation, an additional assumption is required. For this work, the angle α is equal to the angle defined by the UMT, the charge, and the ground ($17.5° \pm 0.5°$). A reasonable assumption considering the axisymmetry of the charge. Solving (9) for V_1, the impulse per area is calculated and results are shown in Fig. 15b. Propagated error in I/A is approximately 1%. The angular location, θ, is determined to within $\pm 0.5°$.

Therefore, the total impulse, summed between the particles and the gas, at the given radius is not discernibly different. While conservation of momentum suggests the lack of differentiation between the bare charges and the particle liner shots is not very surprising, it provides some evidence that a large amount of energy is not absorbed through mechanisms such as fragmentation that could be present in the particle liner shots.

4.3 High-speed images

Figure 16 shows high-speed imagery of the explosive event for the three different test configurations as viewed from Camera 1 (along the long axis of the cylindrical charge). Note that the charge burns toward the viewer from this perspective. The bright explosive products of the bare charge saturate the image and prevent identification of the shock location. However, the explosive product front clearly displays the formation of instabilities as it expands.

For the steel and tungsten liner configurations, a dense soot cloud is formed which obscures the initial development of the particle liner. By 1.2 ms, the tungsten particle liner is visible. At 2.4 and 3.6 ms, the tungsten particles demonstrate the well-known incandescence characteristic of tungsten as it is heated. Some of the tungsten particles seem to track almost simultaneously with the shock front, with a bright, dense band following. After the passage of this bright band, alternating bright and dark striations are present that indicate instabilities in the tungsten particle liner. The steel shot shows different characteristics. Specifically, there is little/no incandescence in the steel particles, and the steel particles appear to travel well behind the shock front.

Figure 17 shows another perspective of the explosive event from the 90° view provided by Camera 3. The charge is burning from right to left in this image. From this orthogonal perspective, the explosive products of the bare charge are restricted to a fairly narrow band with a fireball traveling in the burn direction with a trailing dark soot cloud. The basic form is repeated in the steel and tungsten liner shots, with the exception that the upstream fireball is occluded by a soot cloud after very early times. The still images of the steel and tungsten liner shot reveal the particles are initially occluded by black soot and casing fragments but emerge as time progresses. The tungsten particles incandesce such that the brightness of the particle band increases as more particles become visible. While not as easily distinguishable, the steel particles are a characteristic gray color that emerge from the soot cloud. The brightness of the tungsten particles prevents identifying the case fragments, but they are observed in the

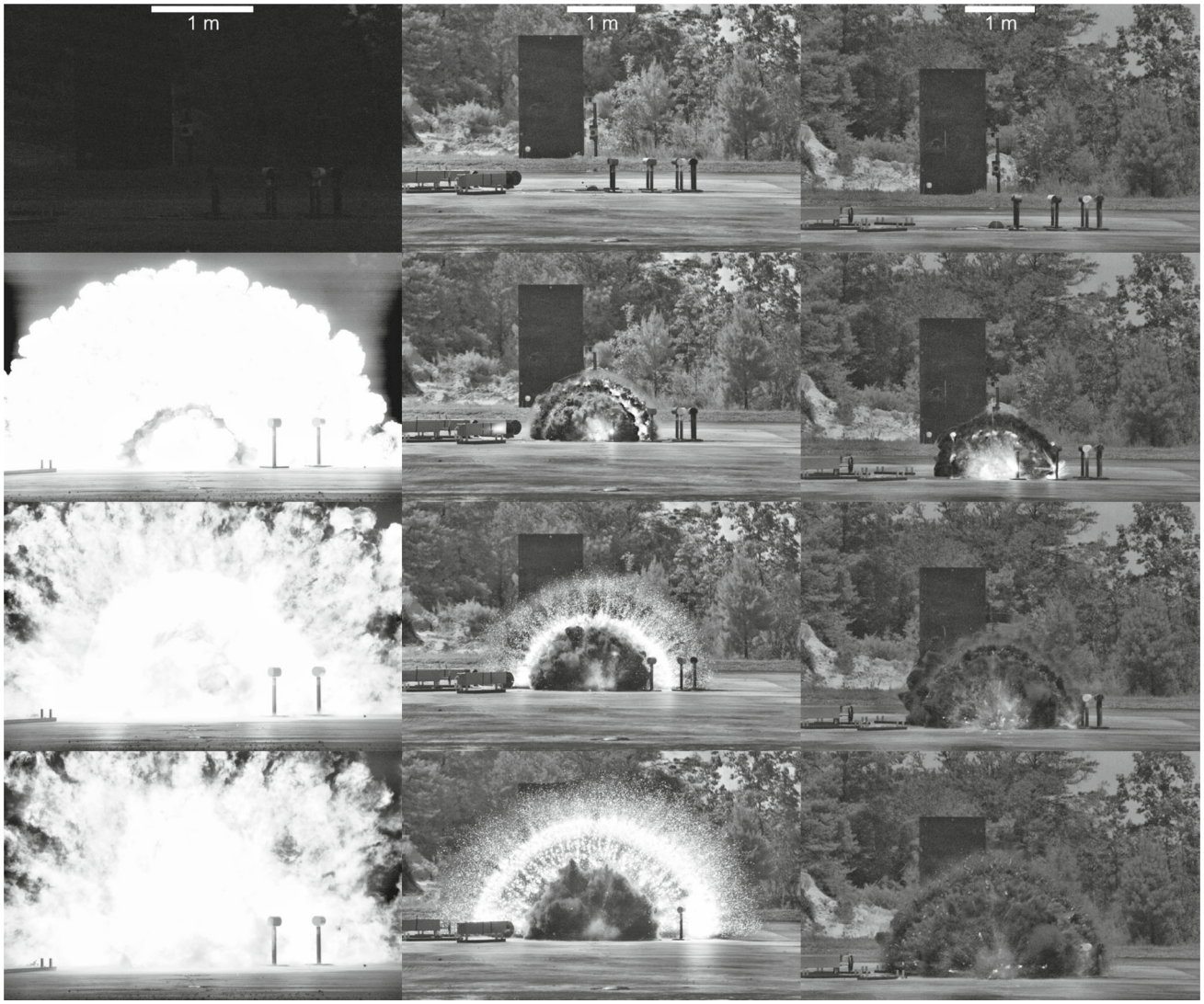

Fig. 16 High-speed imagery of the three test configurations obtained from Camera 1. Time stamps (from top to bottom) are 0, 1.2, 2.4, and 3.6 ms for (left) bare Composition B (center), Composition B with tungsten liner, and (right) Composition B with steel liner. Note magnifications are not equal for all test conditions

steel liner shot to break into many fine strips. From the view shown here, approximately 11 strips are present across the roughly 90° area visible. A total of approximately 44 strips around the circumference of the casing may be estimated to be present, lending further credibility to the previous conclusion that the case notches had no effect. Additionally, the un-notched case in the third steel shot shows similar behavior (not shown).

The experiments done by Frost et al. [14] used a thin disk of glass particles to produce a behavior that is essentially two-dimensional. Therefore, when the camera is located in the axial direction, it was possible to observe the large-scale instabilities. In our steel and tungsten liner shots, the length of the particle liner results in a fully three-dimensional behavior where the instabilities are overlapped with each other, similar to accumulation of numerous two-dimensional phenomena. Therefore, the instabilities are so numerous that they are not easily distinguishable from the next layer of instabilities. Additionally, the amplitude and number of instabilities are not easily measurable.

4.4 Shock tracking

The ToA from the cameras is compared to the pressure probes on the 90° line. Capturing the shocks from multiple perspectives was advantageous. High-speed imagery from the 90° perspective offered by Camera 3 reveals that multiple shock fronts are present. If the shock had only been captured from a single camera, such as Camera 1 or Camera 4, significant

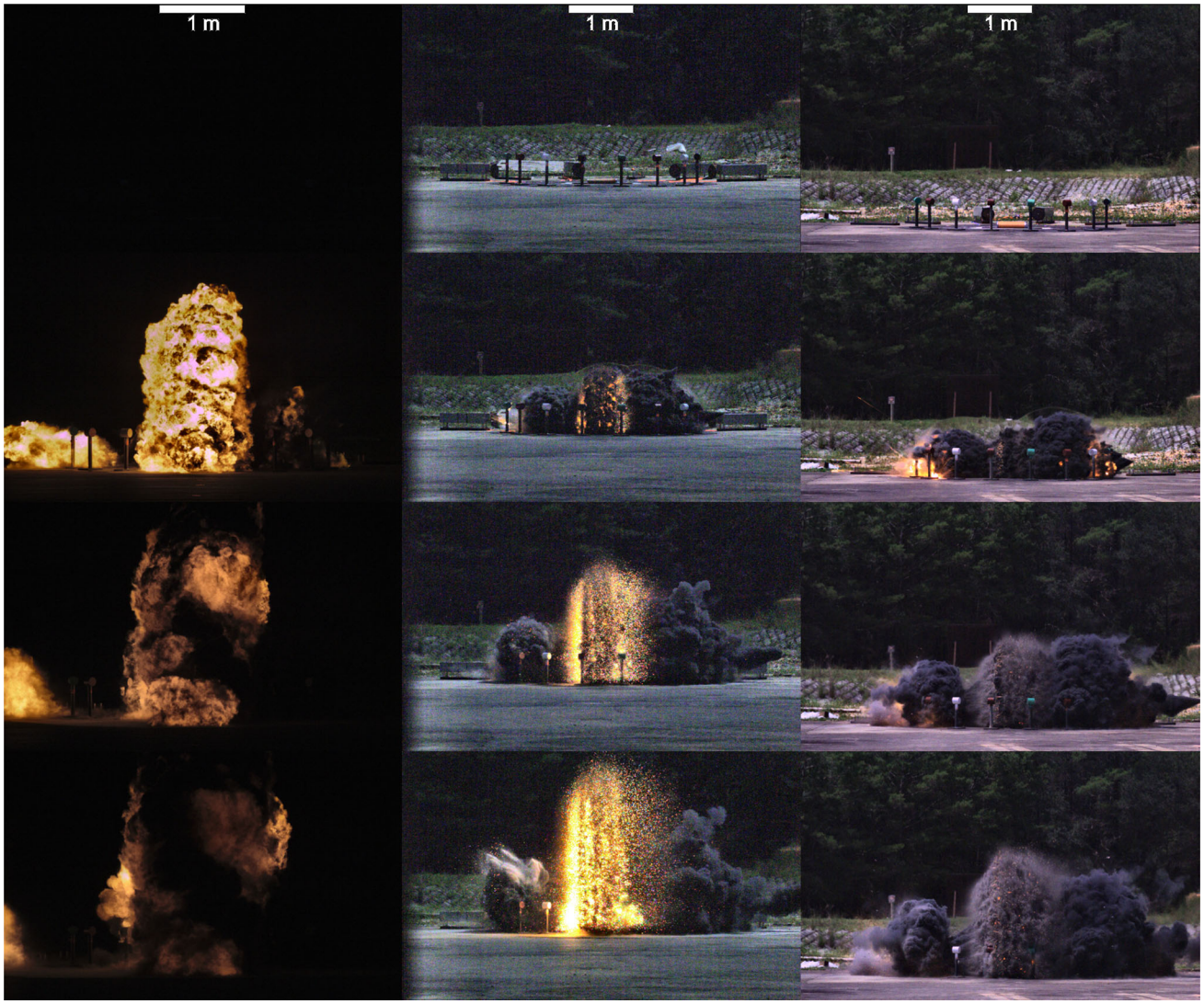

Fig. 17 High-speed imagery of the three test configurations obtained from Camera 3. Time stamps (from top to bottom) are 0, 1.2, 2.4, and 3.6 ms for (left) bare Composition B (center), Composition B with tungsten liner, and (right) Composition B with steel liner. Note magnifications are not equal for all test conditions

bias would have been introduced. The shocks from the ends of the cylinder initially outpace the shock from the center of the cylinder, occluding the location at the centerline. See Fig. 18b for an example of this behavior.

The high-speed videos were analyzed manually to determine the shock location with respect to time. Figure 18a shows an example of the pre-shot image containing the calibration checker fiducial used to establish the spatial resolution for the camera. The fiducial was aligned normal to the camera, and each square in the pattern was nominally 25.4 mm by 25.4 mm. Figure 18b shows an example of the manual selection of the shock for each frame. Low-contrast areas sometimes made the shock unrecoverable against the dark background even with image enhancement. When the shock location was not clear, the frame was skipped, leading to gaps in the data. To determine the precision in the manual shock selection process, the calibration and manual shock selection was repeated three times for each data set in a Monte Carlo fashion. The variability in the shock position results was less than 1%. As a further check against possible bias in shock identification, the Monte Carlo procedure was repeated by an additional researcher. Shock position results by the additional researcher demonstrated approximately 2% variability and overlapped the results from the first researcher. Figure 19 shows the image analysis results for each of the particle liner shots. Results presented are only from the first researcher.

To determine the t_0 of the shock tracking, the frame preceding the frame which first showed light from the detonation was considered the initial time. Accordingly, t_0 uncertainty is equal to the inter-frame temporal spacing of the cameras, approximately 0.1 ms for all four cameras. Shock tracking

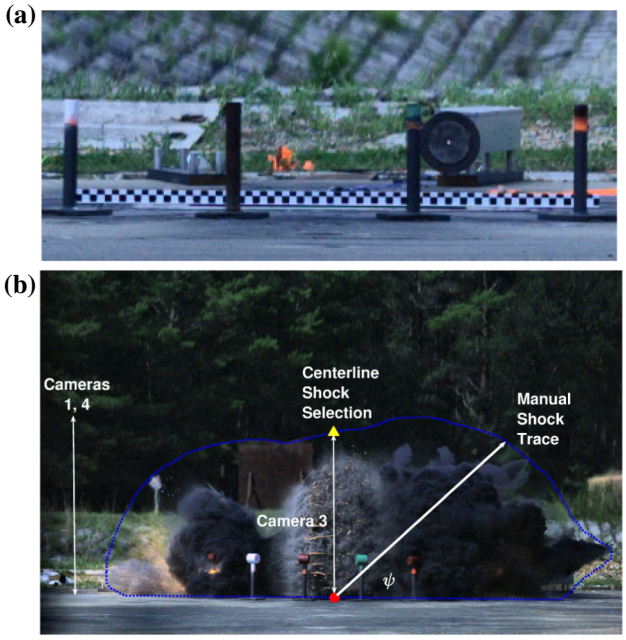

Fig. 18 Image analysis examples. **a** Each camera used a static image with a checker pattern fiducial to calibrate the image. **b** Steel liner shot (Shot 6) 2.7 ms after detonation demonstrates the multiple shock structure observed from the Camera 3 perspective. The charge is burning from right to left in the image. The various camera perspectives record differing shock location results, with Cameras 1 and 4 overestimating the shock location at the centerline. The centerline shock location was selected manually (yellow triangle) as the distance from the charge centroid (red circle). To capture the complex shape of the shock, the shock was manually traced (blue, dotted line) and recorded as distance from the charge centroid with angle ψ from the ground on the right side of the image

results for Cameras 1, 3, and 4 have been included along with the ToA results from the pressure probes orthogonal to the charge. For the tungsten liner configuration, Cameras 1 and 4 appear to better align with the pressure probe results. The steel liner configuration shows that Camera 3 approximately follows the pressure probes for all but the first shot. Camera 1 in the first steel shot departs from the values produced by Camera 4, an unexpected anomaly when comparing the trends of the other three particle liner shots. The cameras viewed the event through mirrors to protect the cameras from shrapnel. The mirrors were replaced between the first and second steel shot. It is likely that Camera 1 had a mirror that was degraded from too much exposure to the sun.

The close agreement between the pressure probes and Camera 3 for the steel shot indicates that ground effects do not significantly affect the ToA for the steel configuration. The tungsten shot exhibits the opposite behavior expected if observing ground effects retard the shock traveling over the pressure probes. The image analysis shows a slower shock traveling normal to the ground.

Finally, Fig. 20 presents an aggregate plot of ToA including the pressure probe and Camera 3 results for all four particle liner shots. Cameras 1 and 4 have been discarded as per the discussion above. The image analysis provides an excellent complement to the pressure probe data, especially by providing data at many more points than the six positions offered by the pressure probes. The results have been zoomed to the first 2 m of the domain.

While less precise than the single-point method above, the shape and position of the shock structure over time was captured with a manual shock trace. The image contrast was adjusted to aid in identification of the shock and then 40–50 points chosen around the perimeter of the shock structure. An example of this process can be seen in Fig. 18. Automated tracing of the shock structure was attempted, but the low contrast of the shock, even after image enhancement, prevented an automated determination of the shock location. Further complicating automation was the presence of many fragments that pierced the primary shock, especially at the ends of the charge, and left significant turbulence in their wake.

The distance between the shock front and the center of the explosive is plotted versus the angular location around the explosive, as shown in Fig. 21. For instance, 0° points to the right of the frame, 90° points vertical, and 180° points to the left of the frame. For the tungsten liner shot, the number of traces was limited to the point at which the bright, incandescent particles began to pierce the primary shock. The brightness of the particles prevented further identification for the low-contrast shock. For the steel liner shots, the shock was able to be identified and traced till the shock began to leave the frame. The bare charge shocks were not visible in any of the frames due to the small aperture used by the cameras, made necessary by the significantly greater amount of light released by the bare charge.

Examining Fig. 21, one may note the inflection points of the three-shock structure observed in Fig. 18b propagate at the same angles to the centerpoint, approximately 80° and 100° after a transitory period of approximately 1.4 ms. Indeed, the shock structure appears to be persistent (except for end effects for angles above approximately 150°) after the transitory period. The tungsten shot appears to be approaching the same behavior, but the traces are likely truncated during the transitory period. Note also that both configurations exhibit a spike in the shock structure due to a large conical soot cloud forming on the left side of the image at approximately 10°. A secondary conical soot cloud of lesser amplitude arises at 40° for the tungsten shot and at 35° for the steel shot (which disappears over time).

4.5 Contact/particle front tracking

The contact front (for the bare shots) and the particle front (for the particle liner shots) at the centerline has been manually

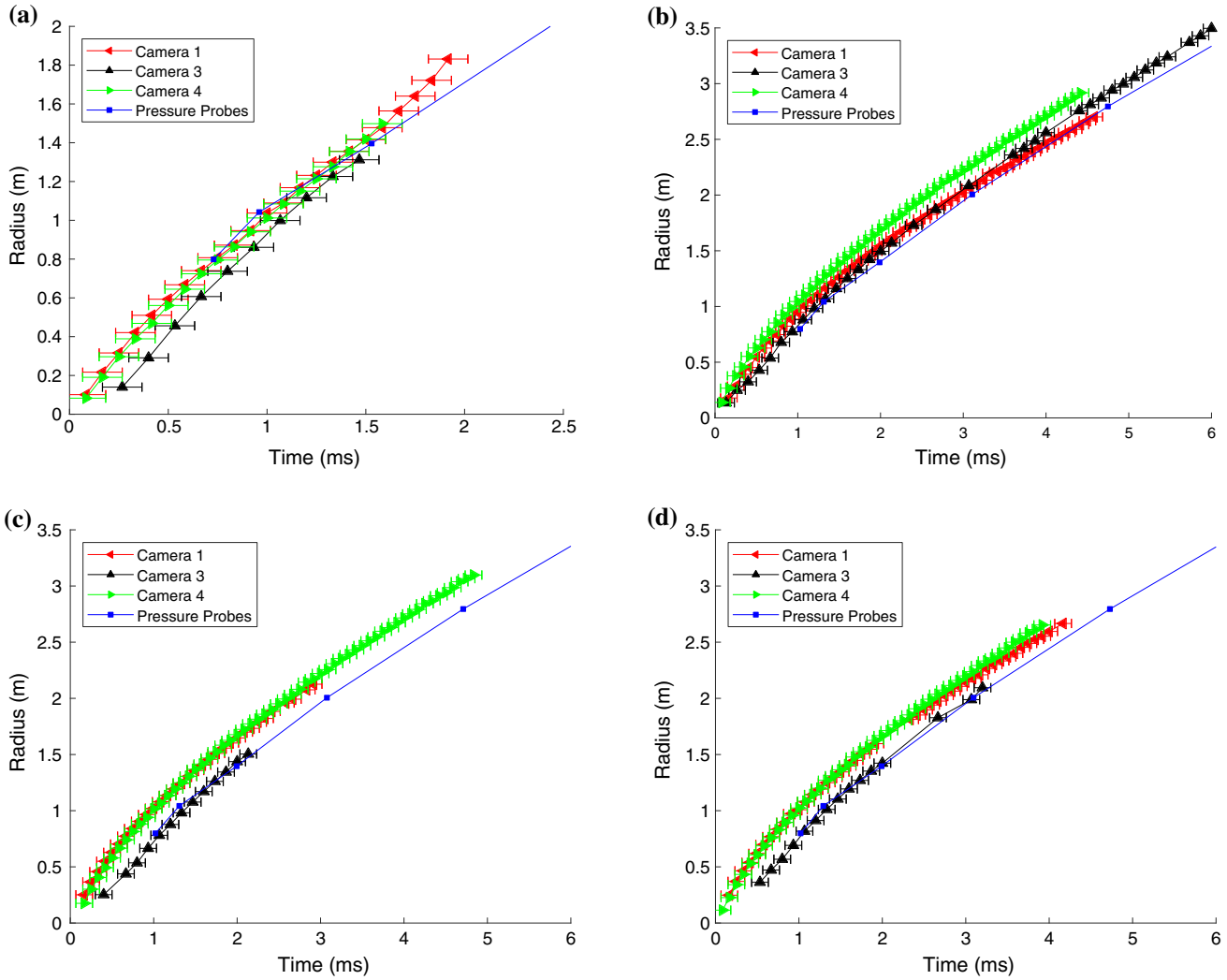

Fig. 19 Shock tracking results at the centerline obtained from the high-speed images using the single-point shock tracking method for **a** Shot 3 (tungsten), **b** Shot 4 (steel), **c** Shot 5 (steel), and **d** Shot 6 (steel). The ToA results from the pressure probes for each shot are plotted for comparison. The data points are connected for convenience of the reader

determined in a similar manner to that pursued for the shock ToA (see Fig. 18b). Figure 22 presents an aggregate plot of the observed contact/particle front compared to the shock ToA as determined by the pressure probes. The particle fronts from Cameras 1 and 4 have been excluded due to the occlusion by the end effects at early time.

To determine the precision in the manual particle front selection process, the Monte Carlo approach detailed in the manual shock selection section was applied. The variability in the contact front position was less than 0.5% compared to the approximately 2% variability in the particle front position.

While less precise than the single-point method above, the shape and position of the particle front was able to be captured automatically. The algorithm used to capture the particle front is as follows. First, the RGB color images were converted to the CIE $L^*a^*b^*$ color space, where L^* is the lightness matrix, a^* is the green-red color component, and b^* is the blue-yellow color component [31]. Second, the absolute value of the difference between the L^* matrix of the dynamic image and the L^* matrix of the static image was computed. Third, the image was segmented using a threshold operation. If the absolute difference exhibited a value greater than a threshold value (which was iteratively determined by the user), the pixel was set to 1. Otherwise, the pixel was set to 0. The threshold value was tuned frame-by-frame to accurately capture the front with typical values between 11–60% for the contact front and 5–15% for the particle front. Fourth, two passes of a 3×3 median filter were applied followed by a 10×10 median filter pass to remove spurious detections. Fifth, holes within the regions were closed using the *imfill* function in MATLAB. Finally, the front position was calcu-

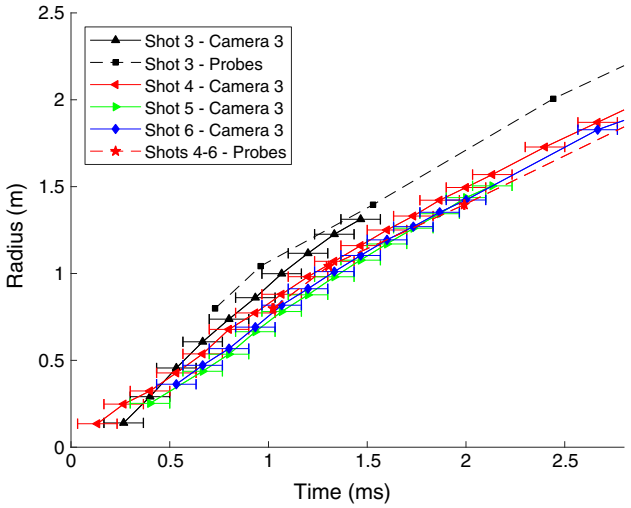

Fig. 20 Aggregate plot of shock time of arrival for all four particle liner shots with comparison to pressure probe results. The pressure probe results for the three steel shots are averaged and plotted with uncertainty bars

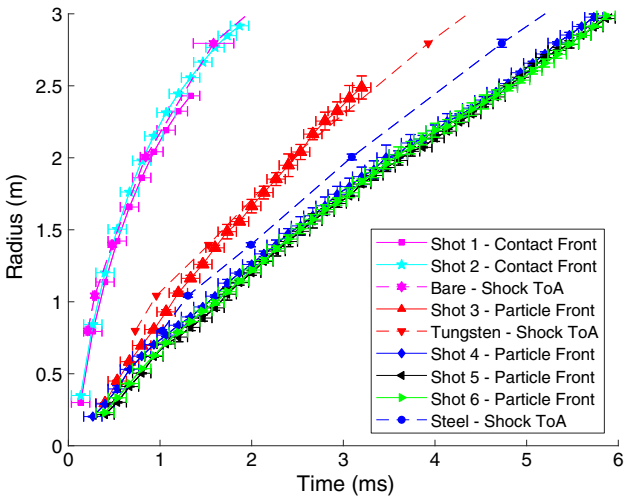

Fig. 22 Aggregate plot of the contact/particle front for all six shots with comparison to the shock ToA obtained from the pressure probes. The pressure probe results for the two bare shots and three steel shots are averaged and plotted with uncertainty bars

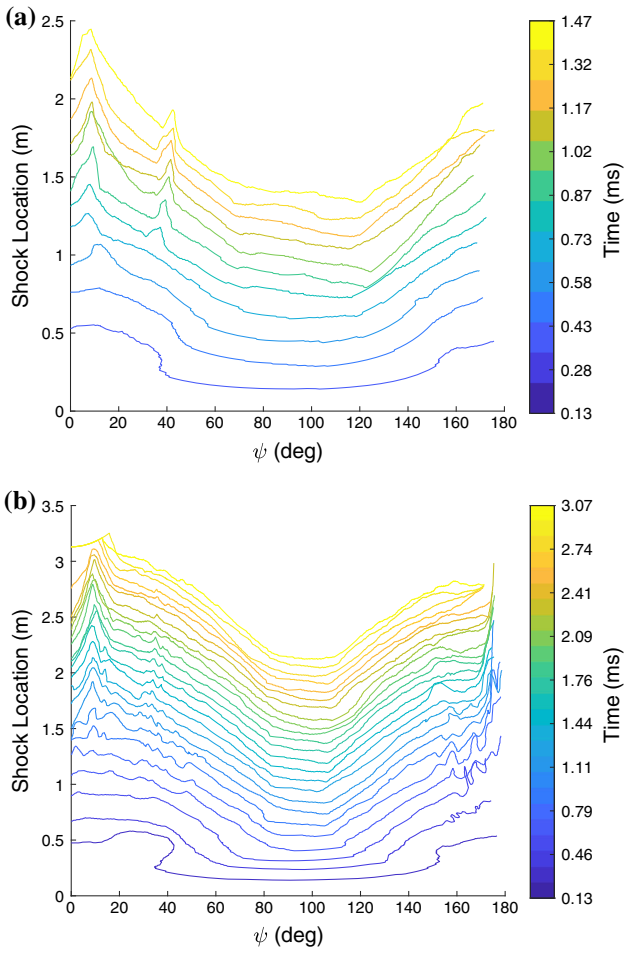

Fig. 21 Manual trace results of the shock structure. **a** Tungsten liner shot (Shot 3). **b** Steel liner shot (Shot 4). Note the color bars are not held constant between plots. The reader is reminded that the charge is end initiated at ψ equal to 0°

lated as the distance from the centerpoint to the boundary of the identified region. Results are plotted using the same angle convention, as shown in Fig. 18.

The results of the particle front algorithm are shown for three of the shots, one for each configuration, as shown in Fig. 23. In contrast to the shock trace results (Fig. 21), results for angles less than 60° and greater than 120° are excluded for clarity. In an effort to accurately capture the shape of the front, threshold values were chosen which resulted in large portions of the black soot clouds to be missed because of their poor contrast with the dark background. Note the algorithm was terminated when the contact/particle front began to leave the frame.

Examining Fig. 23, the contact/particle fronts appear to maintain a persistent shape after a transitory period, similar to the recovered shock profiles. For the contact, the transitory period is short, only about 0.5 ms. When interpreting the particle fronts, the reader is advised that at early time the "particle front" recovered is the black soot cloud. The tungsten particles do not completely emerge from the soot cloud until approximately 1.5 ms. The tungsten particle front profile appears to achieve its persistent shape shortly after the emergence of the particles, though incandescence make the tungsten particle fronts significantly more stochastic than the contact or steel particle fronts. The steel particles completely emerge from the soot cloud at 2.4 ms, but the persistent shape does not appear to be achieved until 3 ms.

5 Conclusions

A rich set of validation data has been provided to the multiphase flow community. Six total explosive tests were

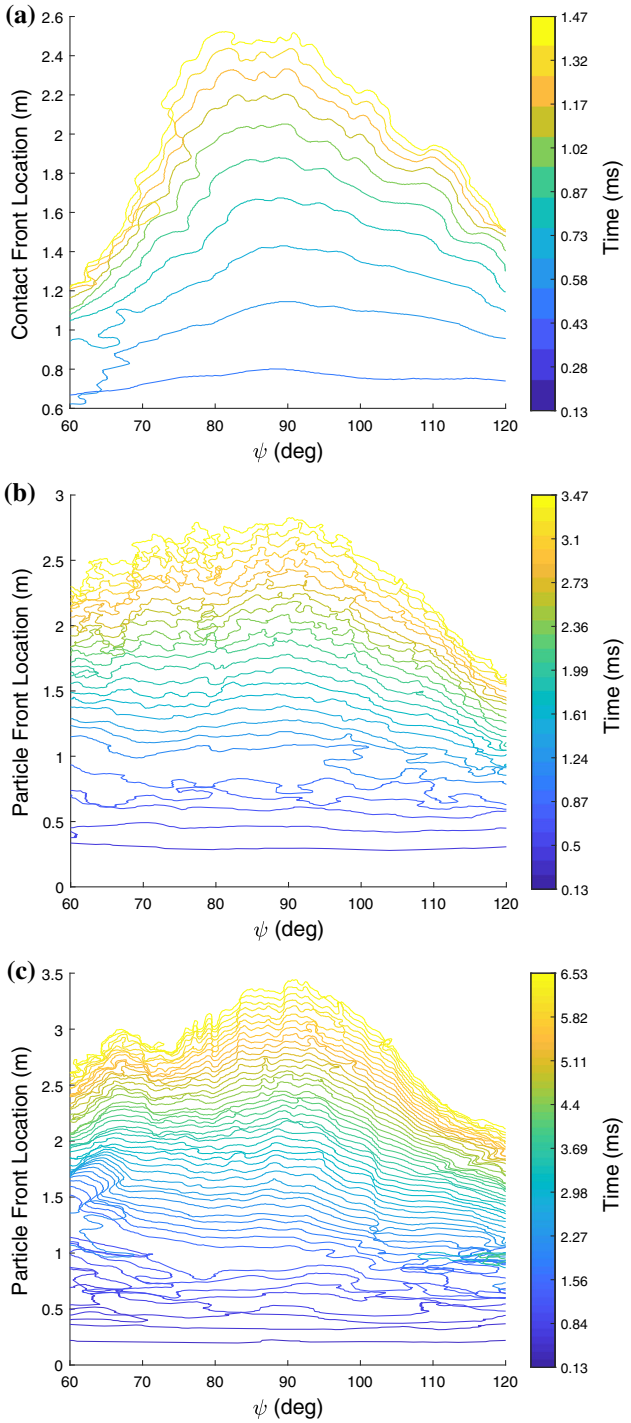

Fig. 23 Contact and particle fronts obtained from the algorithm detailed in the body of the paper. **a** Bare charge (Shot 1). **b** Tungsten liner shot (Shot 3). **c** Steel liner shot (Shot 4). Note the color bars are not held constant between plots. The reader is reminded that the charge is end initiated at ψ equal to 0°

conducted: two bare charges, one tungsten liner, and three steel liners. Careful emphasis was placed on design of the experiments to allow ease of simulation, uncertainty quantification of experimental inputs, and extraction of prediction metrics. Of the various concerns addressed in the design of the experiments, two are of special note. First, it was desired to decouple the structural and fluid dynamics of the problem by ensuring the casing was negligible. This goal appears to have been met by utilizing a phenolic casing. Introduction of notches in two of the three steel liner casings was not shown to largely affect the shock time of arrival or peak pressure. In addition, the number and location of the instabilities was not observed to correlate strongly with the initial location of the notches. Second, it was desired to provide a baseline of the bare charge, a difficult task with the high cost of each shot. While two tests were able to be conducted with no particle liner, by matching the explosive to previous tests conducted at the AFRL blastpad, the number of baseline explosive tests was increased to four samples. Comparison of the pressure data showed excellent agreement with no apparent bias between the four tests.

Key input parameters were identified and empirically measured for uncertainty quantification. A summary table of the inputs may be found in Table 8. Several findings of note arose from the UQ of the experimental inputs. First, the particle density contained a small, but statistically significant, departure from the manufacturer-reported density. Second, analysis of a series of SEM images showed the particle distribution to contain a bimodal distribution, with many small particles broken off the larger particles. Third, CT scans of mock particle beds quantified the small variation present ($< 0.1\%$) in the local volume fraction. Fourth, the authors note they were unsuccessful in fitting common statistical distributions to the particle size distribution and the local volume fraction, emphasizing the need for their empirical measurement. By providing the empirical distributions of these quantities, simulation engineers may seed their simulations with conditions that match the experiment.

For each test, data were collected from four high-speed cameras, 54 inground pressure transducers, eight UMTs, and several OLEs (which were discarded due to their poor performance). From the high-speed videos, the steel and tungsten liner configurations showed a dense soot cloud that obscured the initial development of the particle liner. After early times, the tungsten particles were incandescent as they dispersed. Some of the tungsten particles seemed to track almost simultaneously with the shock front, with a bright, dense band following. After the passage of this bright band, alternating bright and dark striations were present that indicated instabilities in the dispersing tungsten particles.

The steel shot showed different characteristics. Specifically, there was little to no incandescence in the steel particles and the steel particles appeared to travel well behind the shock front. The steel particles exhibited instabilities closer to those shown in the work of Zhang et al. [12] and Frost et al. [14], with fine fingers racing ahead of the front. The instabilities, however, were so numerous that they are not

easily distinguishable from the next layer of instabilities. Additionally, the amplitude and number of instabilities were not easily measurable.

The P_{peak} field for the bare charge displayed local maxima at the 0°, 90°, and 180° directions, as is typical for a bare cylindrical charge [20,21]. A pronounced local minimum was visible at the 45° line. In contrast, the tungsten and steel liner shots displayed a greatly reduced P_{peak} over the entire measured pressure field. In addition, the 90° line no longer experienced a local maximum but changed to a local minimum for the steel shots. Local maxima were still observed at the 0° and 180° due to the significantly smaller amount of metal present in the end caps and the direction of the burn down the length of the charge.

The eight UMTs measured the total impulse, summed between the particles and the gas, at a given radius and showed it not to be discernibly different. While conservation of momentum suggests the lack of differentiation between the bare charges and the particle liner shots was not very surprising, it provided some evidence that a large amount of energy was not absorbed through mechanisms such as fragmentation that could be present in the particle liner shots.

Redundant measurement of the shock time of arrival at the centerline was obtained from the pressure probes and the high-speed videos. Comparison of the two diagnostics shows excellent agreement for the steel liner shots, providing the potential modeler with high confidence of the result. In addition, as the probes measured the shock along the ground while the camera measured orthogonal to it, the agreement provided evidence that ground effects were not significant. Also notable was the persistent shape of the shock on the millisecond time scale, showing that the shock has not yet become spherical even on relatively long time scales. The contact/particle front measurements were obtained both manually and automatically and provided for comparison to simulation. Finally, while seemingly exhaustive, the authors acknowledge that many details of the experiments were not included here. Potential modelers are encouraged to contact the authors if further information beyond what is presented in this paper is desired.

Acknowledgements The authors would like to acknowledge the efforts of the Eglin AFB experimental personnel for their hard work in conducting the experiments and making the experiments available for use. This work was supported by the US Department of Energy, National Nuclear Security Administration, Advanced Simulation and Computing Program, as a Cooperative Agreement under the Predictive Science Academic Alliance Program, under Contract No. DE-NA0002378.

References

1. Tanno, H., Itoh, K., Saito, T., Abe, A., Takayama, K.: Interaction of a shock with a sphere suspended in a vertical shock tube. Shock Waves **13**(3), 191 (2003). https://doi.org/10.1007/s00193-003-0209-y
2. Tanno, H., Komuro, T., Takahashi, M., Takayama, K., Ojima, H., Onaya, S.: Unsteady force measurement technique in shock tubes. Rev. Sci. Instrum. **75**(2), 532 (2004). https://doi.org/10.1063/1.1641156
3. Sun, M., Saito, T., Takayama, K., Tanno, H.: Unsteady drag on a sphere by shock wave loading. Shock Waves **14**(1–2), 3 (2005). https://doi.org/10.1007/s00193-004-0235-4
4. Britan, A., Elperin, T., Igra, O., Jiang, J.: Acceleration of a sphere behind planar shock waves. Exp. Fluids **20**(2), 84 (1995). https://doi.org/10.1007/BF00189297
5. Jourdan, G., Houas, L., Igra, O., Estivalezes, J.L., Devals, C., Meshkov, E.: Drag coefficient of a sphere in a non-stationary flow: new results. Proc. R. Soc. A Math. Phys. Eng. Sci. **463**(2088), 3323 (2007). https://doi.org/10.1098/rspa.2007.0058
6. Wagner, J.L., Beresh, S.J., Kearney, S.P., Pruett, B.O.M., Wright, E.K.: Shock tube investigation of quasi-steady drag in shock-particle interactions. Phys. Fluids **24**(12), 123301 (2012). https://doi.org/10.1063/1.4768816
7. Bordoloi, A.D., Martinez, A.A., Prestridge, K.: Relaxation drag history of shock accelerated microparticles. J. Fluid Mech. **823**, R4 (2017). https://doi.org/10.1017/jfm.2017.389
8. Hughes, K., Balachandar, S., Kim, N.H., Park, C., Haftka, R., Diggs, A., Littrell, D.M., Darr, J.: Forensic uncertainty quantification for experiments on the explosively driven motion of particles. J. Verif. Valid. Uncertain. Quantif. **3**(4), 041004 (2019). https://doi.org/10.1115/1.4043478
9. Wagner, J.L., Beresh, S.J., Kearney, S.P., Trott, W.M., Castaneda, J.N., Pruett, B.O., Baer, M.R.: A multiphase shock tube for shock wave interactions with dense particle fields. Exp. Fluids **52**(6), 1507 (2012). https://doi.org/10.1007/s00348-012-1272-x
10. DeMauro, E.P., Wagner, J.L., Beresh, S.J., Farias, P.A.: Unsteady drag following shock wave impingement on a dense particle curtain measured using pulse-burst PIV. Phys. Rev. Fluids **2**(6), 064301 (2017). https://doi.org/10.1103/PhysRevFluids.2.064301
11. Kellenberger, M., Johansen, C., Ciccarelli, G., Zhang, F.: Dense particle cloud dispersion by a shock wave. Shock Waves **23**(5), 415 (2013). https://doi.org/10.1007/s00193-013-0432-0
12. Zhang, F., Frost, D., Thibault, P., Murray, S.: Explosive dispersal of solid particles. Shock Waves **10**(6), 431 (2001). https://doi.org/10.1007/PL00004050
13. Frost, D.L., Ornthanalai, C., Zarei, Z., Tanguay, V., Zhang, F.: Particle momentum effects from the detonation of heterogeneous explosives. J. Appl. Phys. **101**(11), 113529 (2007). https://doi.org/10.1063/1.2743912
14. Frost, D.L., Grégoire, Y., Petel, O., Goroshin, S., Zhang, F.: Particle jet formation during explosive dispersal of solid particles. Phys. Fluids **24**(9), 091109 (2012). https://doi.org/10.1063/1.4751876
15. Milne, A., Longbottom, A., Frost, D.L., Loiseau, J., Goroshin, S., Petel, O.: Explosive fragmentation of liquids in spherical geometry. Shock Waves **27**(3), 383 (2017). https://doi.org/10.1007/s00193-016-0671-y
16. Pontalier, Q., Loiseau, J., Goroshin, S., Frost, D.L.: Experimental investigation of blast mitigation and particle-blast interaction during the explosive dispersal of particles and liquids. Shock Waves **28**(3), 489 (2018). https://doi.org/10.1007/s00193-018-0821-5
17. Frost, D.L.: Heterogeneous/particle-laden blast waves. Shock Waves **28**(3), 439 (2018). https://doi.org/10.1007/s00193-018-0825-1
18. Bai, C.H., Wang, Y., Xue, K., Wang, L.F.: Experimental study of detonation of large-scale powder-droplet-vapor mixtures. Shock Waves **28**(3), 599 (2018). https://doi.org/10.1007/s00193-017-0795-8

19. Barreto, M., Ohrt, A., Davis, R.: The AFRL Blastpad 2015: Refinements in Design and Procedures. Technical Report, AFRL/RWML, Eglin AFB, FL (2015)
20. Held, M.: Impulse method for the blast contour of cylindrical high explosive charges. Propellants Explos. Pyrotech. **24**(1), 17 (1999). https://doi.org/10.1002/(SICI)1521-4087(199902)24:1<17::AID-PREP17>3.0.CO;2-D
21. Held, M.: Improved momentum method. Propellants Explos. Pyrotech. **26**(6), 290 (2001). https://doi.org/10.1002/1521-4087(200112)26:6<290::AID-PREP290>3.0.CO;2-4
22. Milne, A.M., Parrish, C., Worland, I.: Dynamic fragmentation of blast mitigants. Shock Waves **20**(1), 41 (2010). https://doi.org/10.1007/s00193-009-0235-5
23. Dobratz, B., Crawford, P.: LLNL Explosives Handbook—Properties of Chemical Explosives and Explosive Stimulants. Technical Report, Lawrence Livermore National Laboratory, Livermore, CA (1985)
24. Zhang, F., Ripley, R.C., Yoshinaka, A., Findlay, C.R., Anderson, J., von Rosen, B.: Large-scale spray detonation and related particle jetting instability phenomenon. Shock Waves **25**(3), 239 (2015). https://doi.org/10.1007/s00193-014-0525-4
25. Heimbs, S., Schmeer, S., Middendorf, P., Maier, M.: Strain rate effects in phenolic composites and phenolic-impregnated honeycomb structures. Compos. Sci. Technol. **67**(13), 2827 (2007). https://doi.org/10.1016/j.compscitech.2007.01.027
26. Dullien, F.A.L.: Porous Media: Fluid Transport and Pore Structure, 2nd edn. Elsevier Science, San Diego (1992). https://doi.org/10.1016/C2009-0-26184-8
27. Annamalai, S., Rollin, B., Ouellet, F., Neal, C., Jackson, T.L., Balachandar, S.: Effects of initial perturbations in the early moments of an explosive dispersal of particles. J. Fluids Eng. **138**(7), 070903 (2016). https://doi.org/10.1115/1.4030954
28. Otsu, N.: A threshold selection method from gray-level histograms. IEEE Trans. Syst. Man. Cybern. **SMC–9**(1), 62 (1979). https://doi.org/10.1109/TSMC.1979.4310076
29. Barrett, J.F., Keat, N.: Artifacts in CT: recognition and avoidance. RadioGraphics **24**(6), 1679 (2004). https://doi.org/10.1148/rg.246045065
30. Thomson, E.: Quantitative microscopic analysis. J. Geol. **38**(3), 193–222 (1930). https://doi.org/10.1086/623710
31. Gonzalez, R.C., Woods, R.E., Eddins, S.L.: Digital Image Processing Using MATLAB, 2nd edn. Gatesmark Publishing, Natick (2009)